공학박사 학위논문

페브리 페로 구조 기반
웨어러블 컬러 가스센서

Wearable Colorimetric Gas Sensor
Using Fabry-Perot Cavity

2022년 2월

서울대학교 대학원

기계항공공학부

김 영 균

페브리 페로 구조 기반 웨어러블 컬러 가스센서

Wearable Colorimetric Gas Sensor

Using Fabry－Perot Cavity

지도교수 안 성 훈

이 논문을 공학박사 학위논문으로 제출함
2021년 10월

서울대학교 대학원
기계항공공학부
김 영 균

김영균의 공학박사 학위논문을 인준함
2021년 12월

위 원 장 _____ 박 희 재 _____ (인)

부위원장 _____ 안 성 훈 _____ (인)

위   원 _____ 차 석 원 _____ (인)

위   원 _____ 전 병 국 _____ (인)

위   원 _____ 양 진 규 _____ (인)

Abstract

Wearable Colorimetric Gas Sensor Using Fabry–Perot Cavity

Young-Gyun Kim

Department of Mechanical and Aerospace Engineering

The Graduate School

Seoul National University

Highly sensitive gas-sensing materials have been developed using nano/microtechnology, and the development of gas sensors in the form of wearable devices is a promising research topic. However, overcoming the sensor's high current consumption and operating temperature remains a challenge in many gas-sensing areas. For resolving these issues, a colorimetric gas sensor that uses the structural coloration of the nano-patterned structure for sensing is emerging as a new alternative. However, lithographic nanopatterning processes are not ecofriendly, and the limitations associated with these approaches make it difficult to fabricate large gamuts of colors. Furthermore, extending the range of applications is difficult owing to problems such as measurement of color changes, data quantification, and angular dependence, and many studies on colorimetric sensors overlook these aspects.

In this study, we developed a colorimetric gas sensor that can respond at room temperature. It is based on a Fabry—Perot cavity and does not require a nanopatterning process. A colorimetric sensor element having a linear change period at a specific wavelength was designed using the finite—difference time—domain method. A mechanism for quantifying signals with low power was developed by combining a colorimetric sensor having the aforementioned characteristics with a photoplethysmogram sensor, i.e., a simple measuring device.

We designed a structure that allows sensor replacement and manufactured a watch—type wearable sensing device that has irreversible sensors and is capable of multi—gas sensing. A gas sensor with a wide concentration range for NO_2 (0.1–500 ppm) at room temperature was obtained, and reliability of >95% was realized in a 5—ppm NO_2 environment using artificial intelligence. Finally, we presented the simplified design of a wearable gas sensor that detects harmful gases using a multilayer color film at room temperature and quantifies color changes using a monochromatic light—emitting diode.

Table of Contents

iv

LIST OF FIGURES

LIST OF TABLES

Chapter 1. Introduction

1.1. Toward wearable gas sensor

Safety accidents at industrial sites due to gas leaks are increasing. Accidents caused by corrosive gases such as NOx and SOx and explosions caused by explosive gases such as H2 threaten the safety of workers (Figure 1). The Severe Disaster Punishment Act was enacted in Korea in 2022, indicating that the prevention of gas-related accidents is becoming more important.

As the performance of gas sensors is improved and they are miniaturized with the development of nano/microtechnology, various wearable gas sensors are being introduced. However, despite dozens of sensors being mounted on smartphones, which are the most representative mobile devices, it remains difficult to apply gas sensors to mobile devices. This is because the conventional chemiresistors and electrochemical and transistor-type gas sensors reduce the use time of the wearable or mobile device owing to the high power consumption and operating temperature (Figure 2). In addition, it is difficult to apply commercial devices due to the size that is hard to be mounted on thin smart devices, the complex

manufacturing process that has not been verified for mass production, and poor environmental resistance.

Flexible, low-power gas sensors have the potential to significantly extend the range of applications of conventional gas-sensing devices [1–3]. In particular, wearable gas sensors can be used in industrial sites and medical applications for safety monitoring [4, 5]. Such monitoring can provide real-time data on field workers, significantly increasing the likelihood of diagnosing toxic gas leak risks early [6]. Ideally, wearable gas sensors should respond at room temperature, consume little power, and have small sizes [7]. Various gas-sensing mechanisms using chemiresistors, electrochemical sensors, transistors, and color changes have been studied. The potential applications these gas sensors for hazardous-gas detection have been extensively investigated [8].

Figure 1 Need for gas sensor [9 − 11]
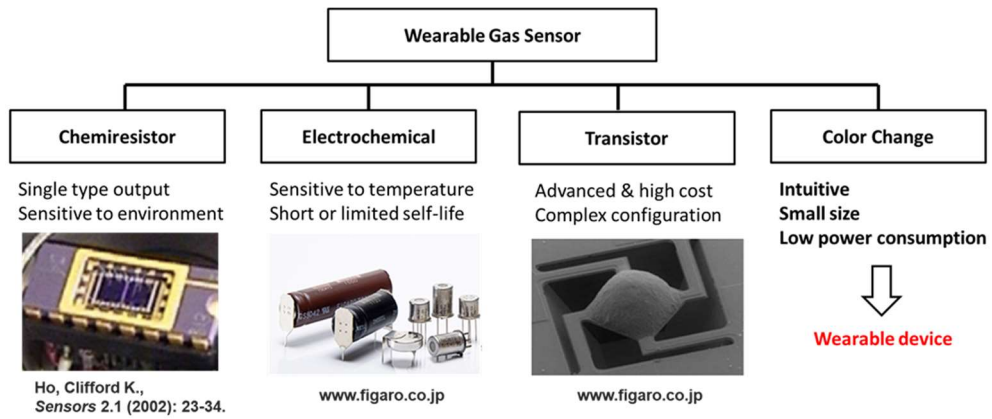
Figure 2 Types of Gas sensor in industry and academy [12, 13]

1.2. Colorimetric gas sensor

Colorimetric gas sensors can be used to visually check the exposure of harmful gases without an external power supply [14]. However, they have not been commercialized, because of the expensive nano/microscale fabrication process, measurement error due to angular dependence, hysteresis due to repeated surface reactions, and deterioration caused by the environment [15–17]. In addition, there is a limitation in that a separate lighting device or a measuring device such as a spectrometer is required for accurate data quantification [18]. The colorimetric gas sensor based on the Fabry–Perot (FP) interferometer is a suitable solution to this problem. The nano- multi-film-based structure is suitable for mass production. The fabrication of the metal–insulator–metal (MIM) structure using electron-beam (e-beam) physical vapor deposition (PVD) or sputter processes and commercially available metal and ceramic materials is a proven process, and sensors of various sizes can be manufactured inexpensively. Methods for detecting various gases such as NO_2 and H_2 in color at room temperature using the change in the thickness of the upper metal layer or the change in the thickness or refractive index of the insulator have been reported [19–

21].

Simpler methods for measuring the color change of a color sensor have also been reported. The color change causes a spectral change of the reflected wavelength, and if the change in reflectivity in a specific wavelength band is constant, a high-quality signal can be obtained with a simple device without a spectrometer. For photoplethysmogram (PPG) sensors using monochromatic light-emitting diodes (LEDs), one attractive approach is to measure the color change using a simple device [22]. Combining a colorimetric sensor with a monochromatic LED allows signal quantification with a simple structure and low power consumption. In addition, the angular dependence can be reduced with a simple structure.
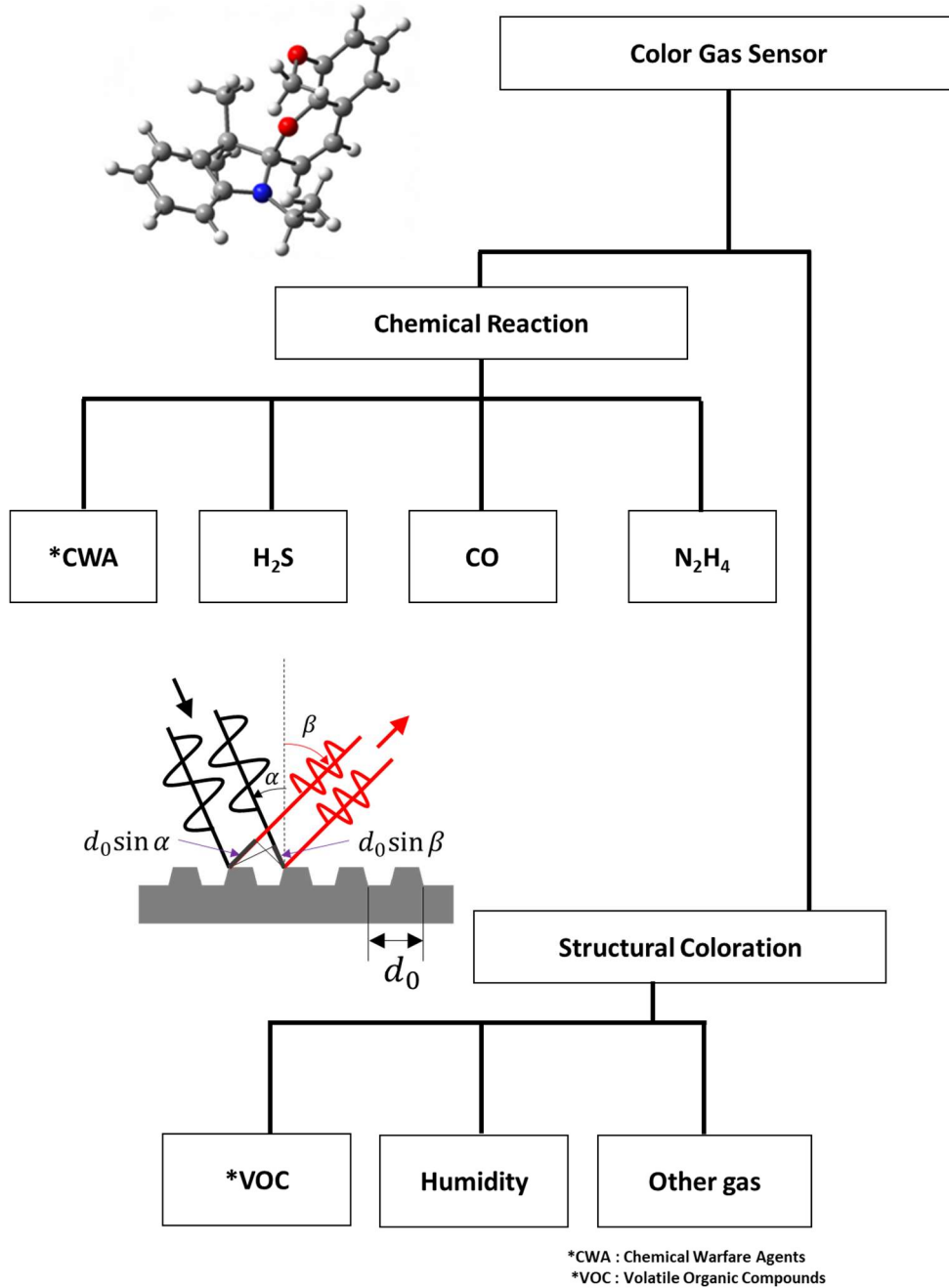
Figure 3 Types of Colorimetric gas sensor

1.3. Research Objective

Sensitivity, selectivity, and reproducibility are fundamental requirements for gas sensors. For applying a new gas sensor to a wearable device, the following additional requirements must be satisfied.

1. Room-temperature sensing: 20–25 ℃
2. Low power consumption: <20 mW
3. Small size: under 0.3 t

In this paper, a colorimetric gas sensor coupled with a PPG sensor is proposed as a sensitive NO_2 gas sensor. For the FP interferometer (FPI)-based colorimetric sensor manufactured using e-beam PVD, the nonlinearity of the fabrication process is minimized by controlling the evaporation rate. The FPI sensor is designed using the finite-difference time-domain (FDTD) method so that the color change can be easily observed with the naked eye and has a linear reflectance change value at a wavelength of 660 nm. The FPI sensor combined with the PPG can be operated at room temperature and has low power consumption of <1 mW; thus, it can be used as a wearable

gas sensor. The proposed gas sensor can detect accumulated NO_2 gas in industrial sites at a level of 0.1 ppm and can monitor NO_2 concentrations of >5 ppm in real time using a long short-term memory (LSTM) model. A wearable device for workers was manufactured, and a real-time harmful-gas monitoring system using it was proposed.
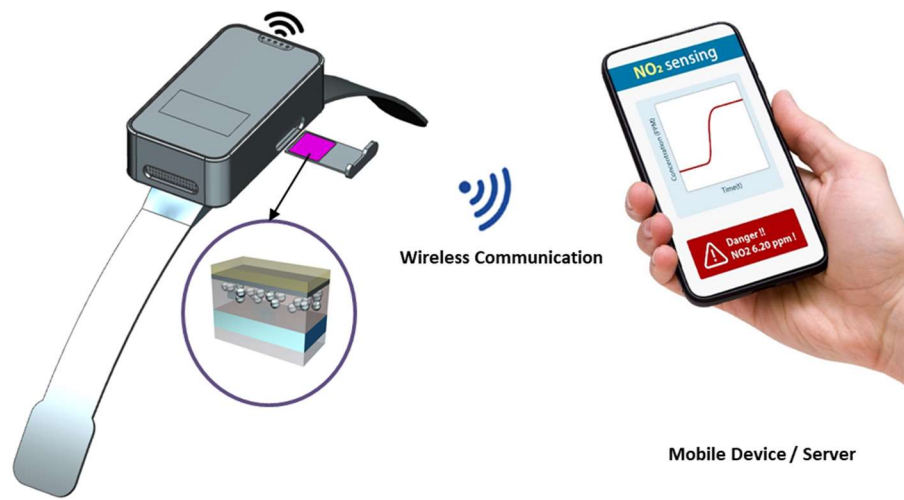
Figure 4 Schematic of watch type wearable gas sensor

Chapter 2. Fabry-Perot Color

2.1. Fabry-Perot Cavity

In the case of localized surface plasmon resonance, which provides color for nanostructures, FP interferometry via nanoscale thin-film deposition of metal and insulator layers is a more readily accessible method for fabricating large-area nanostructures [23]. This type of interferometer usually has an MIM structure, in which mirrors on both sides of the device are mostly composed of metal, while the intermediate resonance layer constitutes an insulator [24, 25]. A more reasonable method for realizing structural coloration, i.e., stacking two-dimensional nanostructures, has already been commercialized and allows precise control of the thin-film thickness through lithography or e-beam-based processes [26, 27]. These methods are highly advantageous for obtaining large areas of color and are therefore used in industry for the surface treatment of electronic devices and the production of display materials [28].
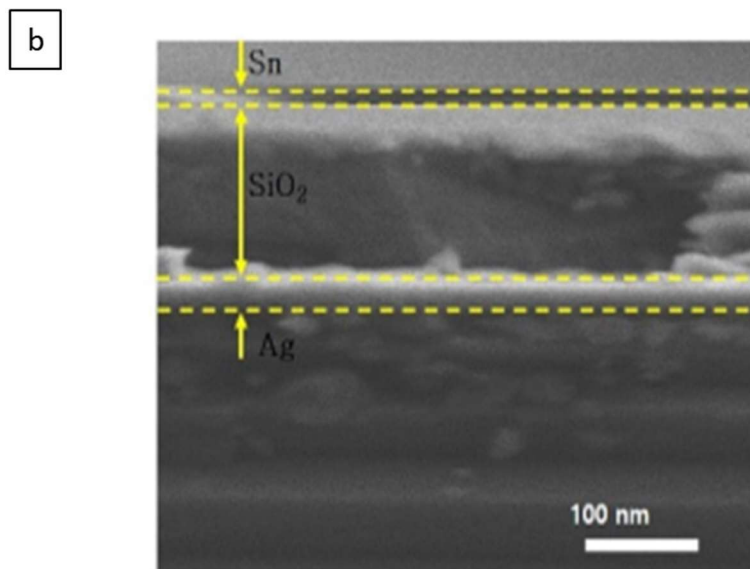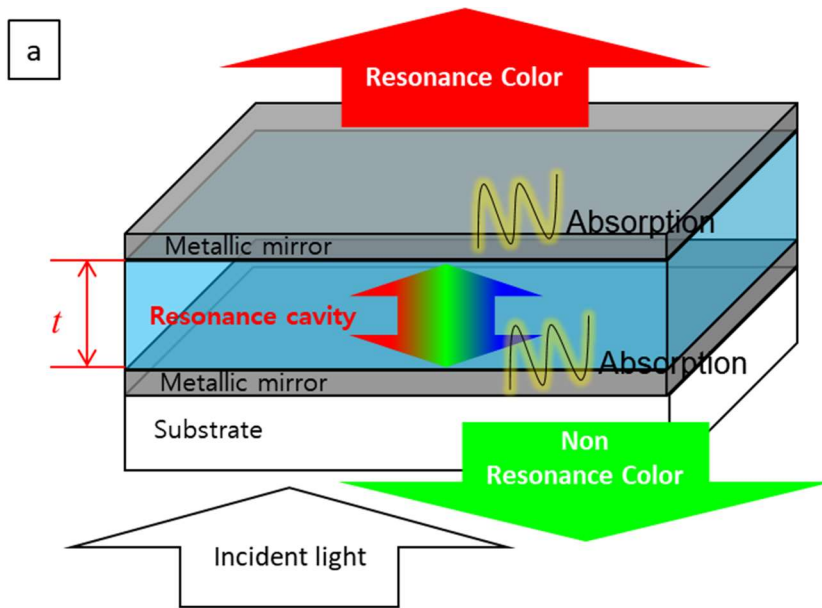
Figure 5 Fabry − Perot cavity using MIM structure a. schematic of MIM structure b. Transmission electron microscopy image of MIM structure

2.2. Design using FDTD

The FPI can be explained with wave optics, but the color is a combination of visible layers with wavelengths between 400 and 700 nm. Thus, Maxwell's equations are used (as described below) to include the optical properties of all the visible layers' wavelength bands. The FDTD method is used to solve Maxwell's equations discretely.

Figure 6a presents the concept of FDTD analysis and the solution for the difference in the electric field before and after the ray passes through both mirror surfaces using the finite-difference method. After the nodes are installed before and after the mirror layer and the insulator, the finite-difference method is implemented along the direction of light [29].

Figure 6b shows the FDTD analysis results for structures of Ag 50 nm-SiO2 (0-400 nm)-Sn (10 nm) and Ag 50 nm-SiO2 (0-400 nm)-Ag 30 nm. The magnitude of the reflectivity of light in the visible ray region is expressed as one graph. So, it visually expresses the optical change due to the difference in the thickness of the mirror layer.
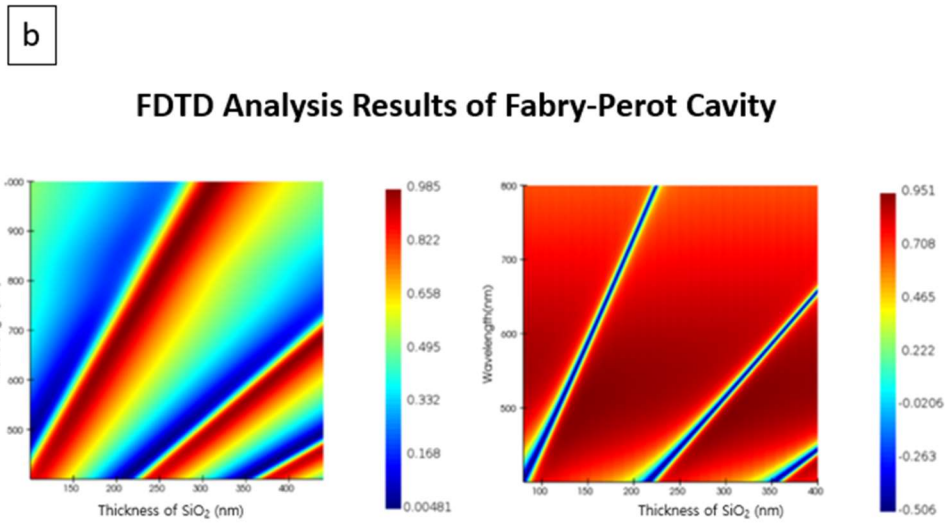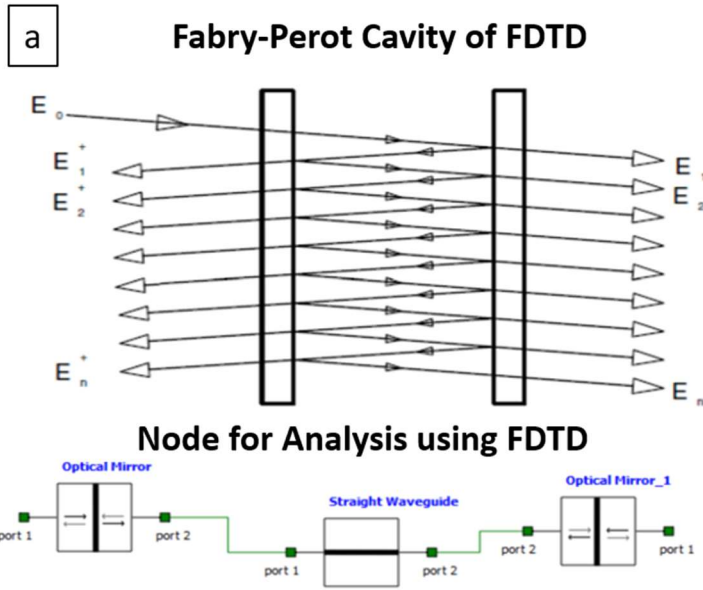
Figure 6. FDTD analysis of Fabry−Perot cavity a. schematic of Fabry−Perot cavity b. FDTD analysis of Fabry−Perot Cavity [24] of Ag 30 nm −SiO₂ (100~450 nm)−Sn 10 nm (left) and Ag 30 nm − SiO₂ (100~400 nm)− Ag 30 nm (right)

2.3. Design criteria of Fabry—Perot sensor

The human eye, which detects color with cone cells, is most sensitive at 550 nm. Therefore, color changes in the colorimetric sensor using the FP cavity can be easily detected by the human eye when the change in wavelength occurs around 550 nm. Figure 7a presents the thin—film interference equation [30].

$$p \; = \; 2 \, n_f \, d \, \cos \theta \text{-----------------------------}(2\!-\!1)$$

(n_f = refractive index of film, d = thickness of insulator, θ = angle of incident light)

Here, the refractive index (n_f) cannot be adjusted, and the angle (θ) of the incident light is not suitable as a design variable for a colorimetric sensor that must have a wide viewing angle. Therefore, in FP—cavity design, it is important to shift the center of the absorption peak to 550 nm by changing the insulator thickness (d), as shown in Figure 7b.

Thin Film Equation

Incident light　Reflected light

$P = 2n_f d \cos \theta_2$

θ_1

n_0

n_f

θ_2

d

Transmitted light

Center Peak Shift to 550 nm

Reflectance (a.u.)
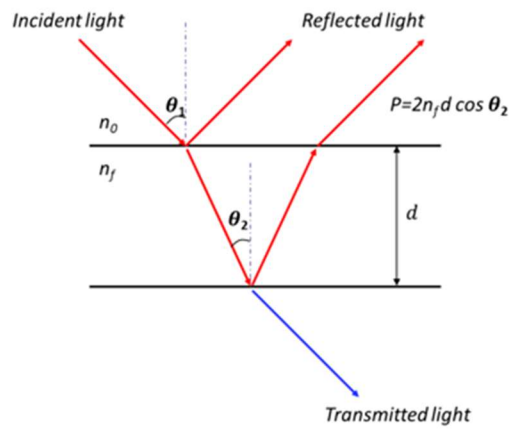
wavelength (nm)

Figure 7 Center peak design a. Thin film equation b. center peak shift to 550 nm using thickness change of insulator layer

Next, by controlling the mirror thickness, the visibility of the structural color can be designed. In the case of a colorimetric sensor with reflective color, colors with wide peaks are seen more clearly [31] (Figure 8a). It is important to drop the fine value (F) for a color with a wide peak [30].

$$F = \frac{4r^2}{(1 - r^2)} \quad \text{--------------------------------} (2-2)$$

According to the equation for the finesse value, the reflectivity of the Ag mirror layer should be low. Additionally, the reflectance of the Ag mirror layer depends on the wavelength, and we tune the visibility using the FDTD method with the change in reflectance by the adjusted thickness (Figures 8b and 8c).
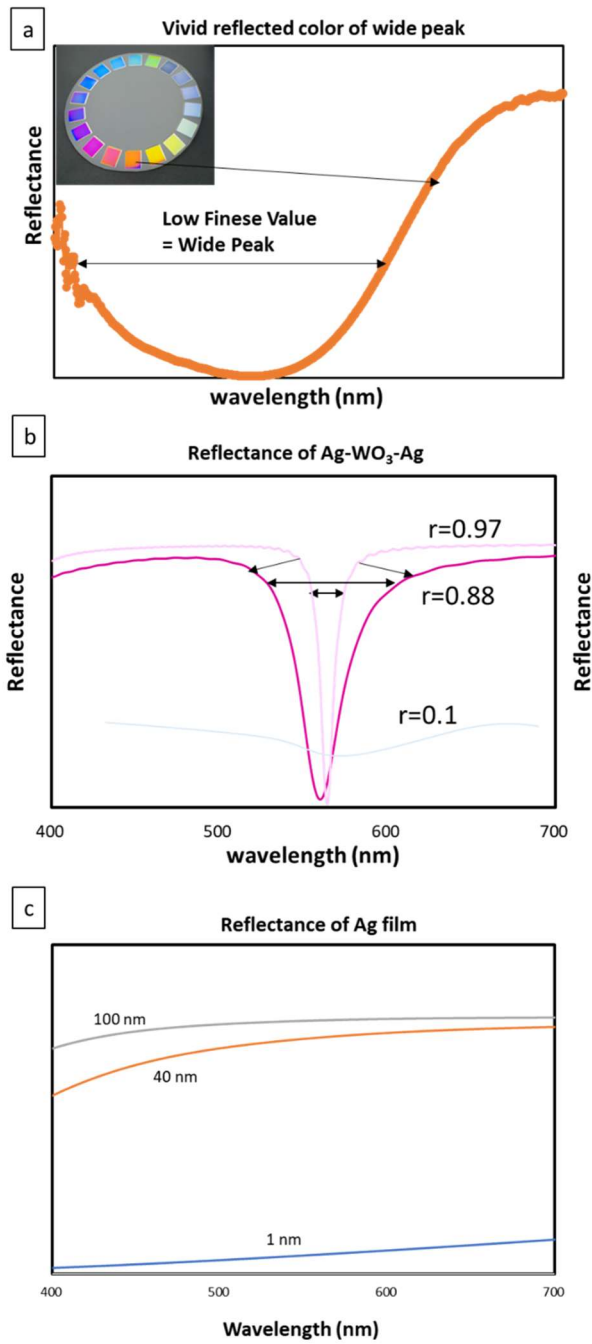
Figure 8 Reflected color of MIM a. Vivid reflected color of wide peak, b. Reflectance of Ag $-WO_3-$ Ag thin film c. Reflectance of Ag thin film

Figure 9 shows the narrow- and broad-peak models designed using the FDTD method. The narrow-peak model is preferred for applications using transmitted colors. Owing to the high reflectance of the thick mirror layer, the absorption peak of the FB cavity is narrow, and the visibility of the reflected color is poor.

The broad-peak model uses an asymmetric thin mirror layer to enhance the visibility, and the FB cavity is designed with an absorption peak in the 550-nm region by adjusting the insulator thickness of WO_3 material. Thus, the color is more vivid than that of the narrow-peak model.

In the case of the broad-peak model, the reflectance change according to the Ag thickness change at 660 nm is large and uniform. Using this characteristic, the color change of the colorimetric sensor can be determined even via single-wavelength measurement.
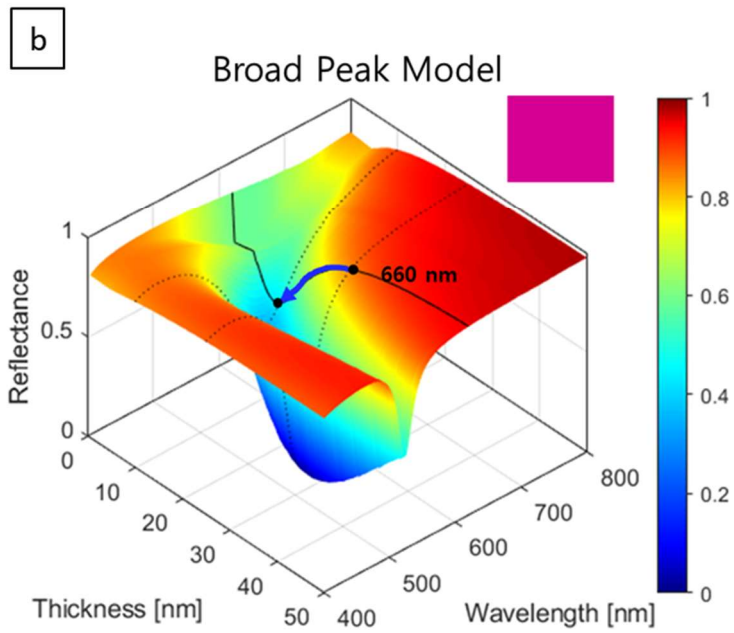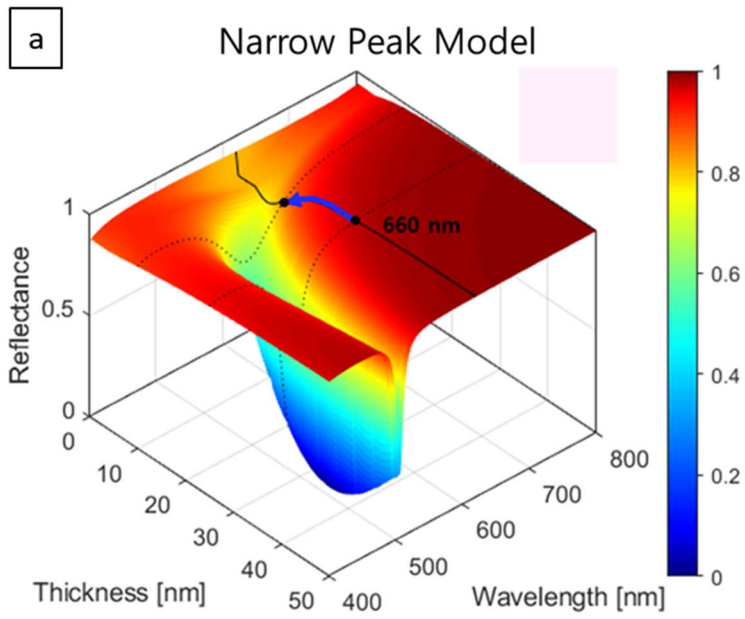
Figure 9. a. Narrow peak design b. broad peak design of FB cavity

2.4. E-Beam based nanomaterial evaporation

The e-beam method is widely used for thin-film deposition in industry (Figure 10). The advantages of the PVD method include the high speed and the use of various deposition targets. The process of fabricating the sensor starts with mask manufacturing. First, a mask is manufactured, attached to the substrate, and placed in the substrate holder inside the evaporator. Numerous thin-film samples can be manufactured, depending on the size of the deposition furnace. After the deposition target substrate is mounted on the substrate holder, the crucible containing the deposition target is placed in the concave part of the e-beam module. The crucible material is selected as graphite or ceramic depending on the melting point of the target material. Cooling water flows around the crucible, and a high-intensity e-beam (3–20 kV) is focused and irradiated, it prevents the damage caused by heat. High-energy electrons fly upward from the filament of the electron gun and are bent by the magnetic force, hitting the target. The deposition rate is determined by the degree of vacuum and the electron energy applied to the target.
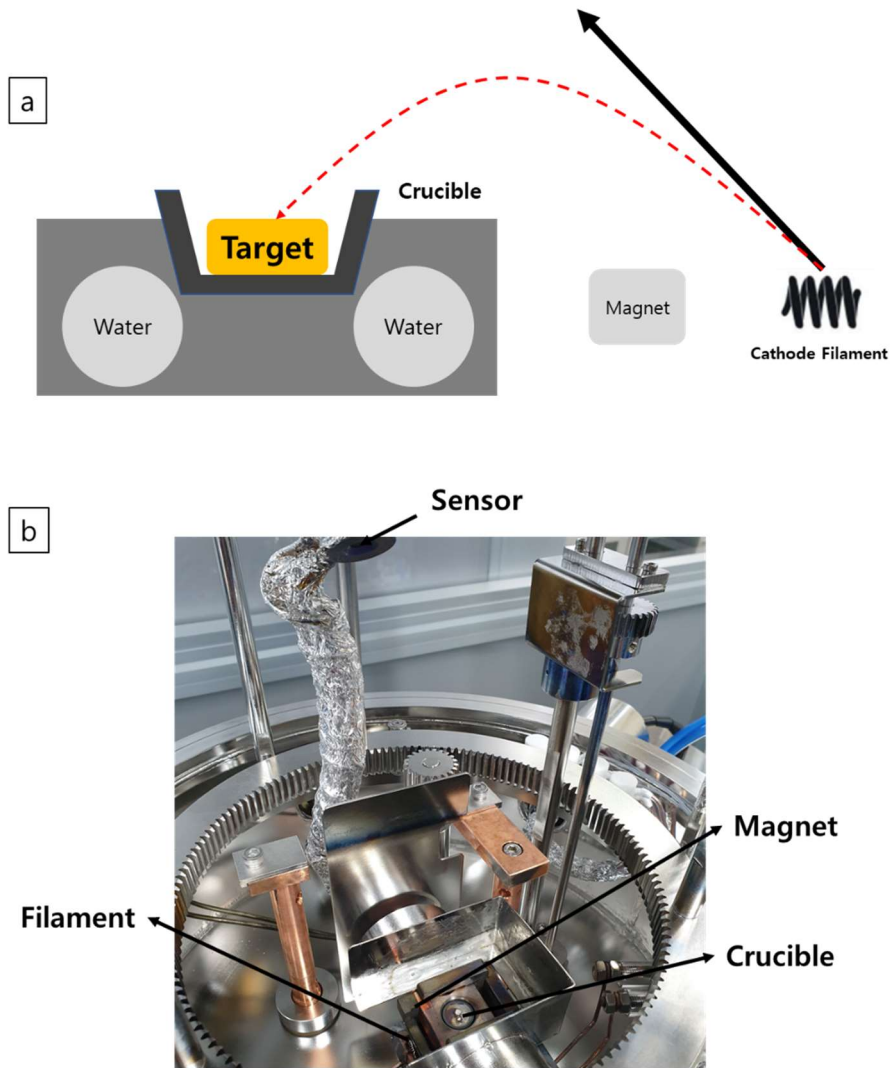
Figure 10 e−beam PVD (a) E−beam evaporation mechanism (b) E−beam evaporator inner structure

2.5. Evaluation and adjustment of e-beam PVD

In the e-beam PVD process, which is the manufacturing process for colorimetric gas sensors, managing the accuracy of the film thickness is important. Owing to the characteristics of the FP cavity, the error between the mirror and the insulator thickness degrades the reliability of the sensor performance. For accurate thickness measurements at the nanoscale, cross-sectional analysis using transmission electron microscopy (TEM) is required. However, this method is expensive, and for non-conductive materials, material changes may occur during the TEM sample fabrication process. To solve these problems, an FDTD simulation is used.

Figure 11 shows the steps of the fabrication process and the modulation of the tooling factor for the e-beam evaporation process. The 1st color element is fabricated according to the designed structure. The thickness of the e-beam evaporator is measured as follows. When the density and z-factor value of the deposition target material are input, the sensor detects the accelerations at which the nanoparticles collide as they evaporate and integrates them to calculate the thickness.

The spectrum of the fabricated sample is measured using a spectrometer. After the tooling factor of the e-beam evaporator is adjusted by comparing the measured spectrum with the spectrum calculated via the FDTD method, an improved sample is fabricated. Through this method, the fabrication process can be optimized without analyzing the sample using the TEM, which is expensive. Additionally, the method can be used to manufacture Colorimetric sensors with accurate specifications.
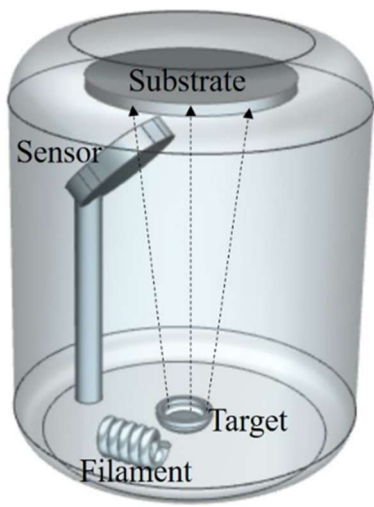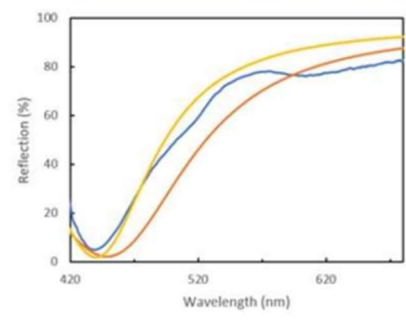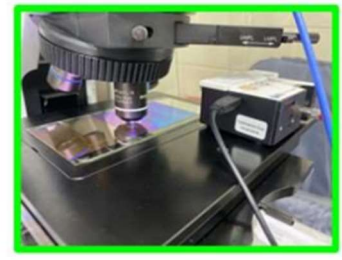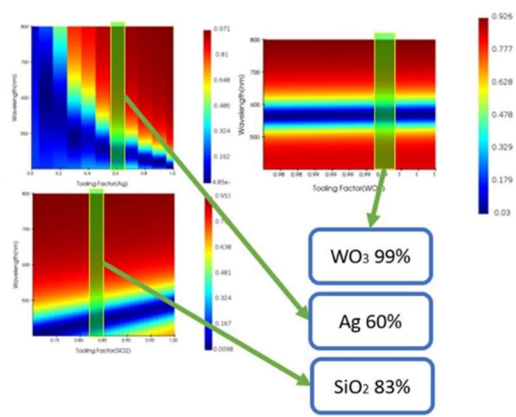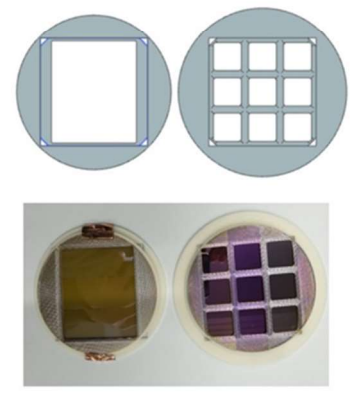
Figure 11 The steps of fabrication process and the modulating tooling factor of e−beam evaporation process

Chapter 3. NO$_2$ Gas Sensor

3.1. NO$_2$ Gas Sensor and Sensing Mechanism

NOx gas is a colorless, odorless, and harmful gas that is toxic to human lungs even in small exposure amounts. In various applications, e.g., the manufacturing industry and first-responder use, NOx gas sensors can provide essential information.

Figure 12a shows a film-type NO$_2$ colorimetric gas sensor with an MIM structure that produces FP resonance. NO$_2$ gas reacts with moisture in the air to generate HNO$_2$ and causes a corrosion reaction in the Ag layer on the upper layer of the MIM structure. The following equations describe the corrosion reaction between Ag and NO$_2$ [32].

$$3 \ NO_2 \ (g) + H_2O = 2H+ + 2NO_3- + NO(g) \ \text{--------}(3-1)$$

$$2 \ NO_2 \ (g) + H_2O = H++NO_3- + HNO_2(g) \ \text{--------}(3-2)$$
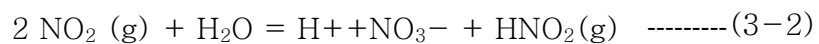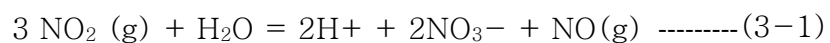
When the thickness of the upper mirror layer of the MIM structure decreases owing to corrosion of Ag, the color of the colorimetric gas sensor is changed. WO3 was selected because it has

a larger refractive index than other insulators and thus exhibits a large color change even with a thin mirror layer (Figure 12b).

Most gas sensors with an FB-cavity structure induce color change mainly by changing the thickness of the insulating layer or changing the refractive index. In contrast, we present a novel sensing mechanism—an FP cavity gas sensor that represents the corrosion of its top metal layer as a drastic color change based on the concentration of the corrosive gas at room temperature. Because all the layers of the MIM structure (except for the top layer) are protected from the corrosive gas by the upper layer, the sensor parameters affected by the gas are independent and can be simplified. Therefore, this mechanism provides an advantage for analyzing changes in the optical properties of the sensor.

The MIM structure was designed, and its reflectance was calculated as follows [33].

$$R = \frac{4r\,sin^2\delta}{(1-r)^2 + 4r\,sin^2\delta} \quad \text{------------------------}(3-3)$$

Here,

- r_i represents the reflectance between the medium and the cavity, and

- δ ($\delta = 2\pi nd/\lambda$) represents the phase difference, with n being the refractive index, d being the cavity length, and λ being the wavelength.
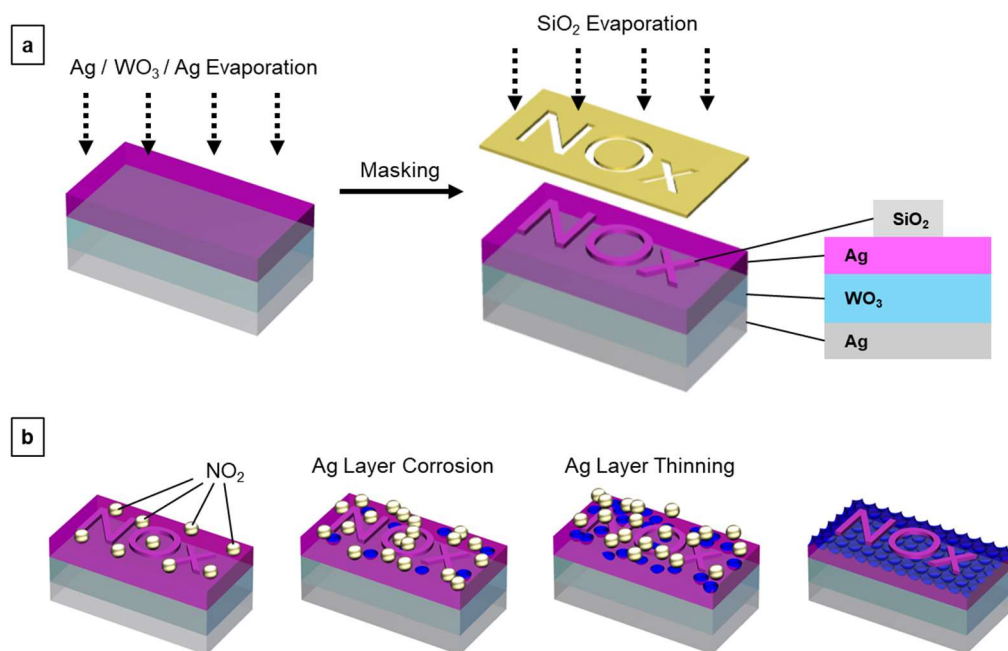
Figure 12 schematic design of the proposed gas sensing device

3.2. Sensor Design using FDTD

Figure 13a shows the results of the FDTD method for the color change that occurs when the NO_2 sensor reacts with gas. The bottom Ag thickness was fixed at 40 nm, and the spectrum of the FB cavity with Ag and WO_3 layer thicknesses of 0 – 30 and 0 – 100 nm, respectively, was analyzed. A basic requirement of a colorimetric gas sensor is that the color change can be easily checked with the naked eye without a measuring device. Cone cells, which distinguish colors in the human eye, can most sensitively recognize changes at wavelengths near 550 nm. Hence, WO_3 and Ag layer thicknesses of 70 and 30 nm, respectively, which were the most sensitive to color change in the 550 nm region of the sensor design, were selected [19] (Figure 13a).

Regarding the spectral change of the colorimetric sensor, it was confirmed that the reflectivity decreased as the Ag layer became thinner in the long-wavelength region of $\geq$ 650 nm (Figure 13b). Figure 13c presents the reflectivity in the 660 nm region; as shown, the color changed from purple to light blue, and the reflectivity was constant.

Therefore, the reduction in the Ag thickness can be measured in PPG

using a monochromatic LED or a laser having a light－emitting part of 660 nm.
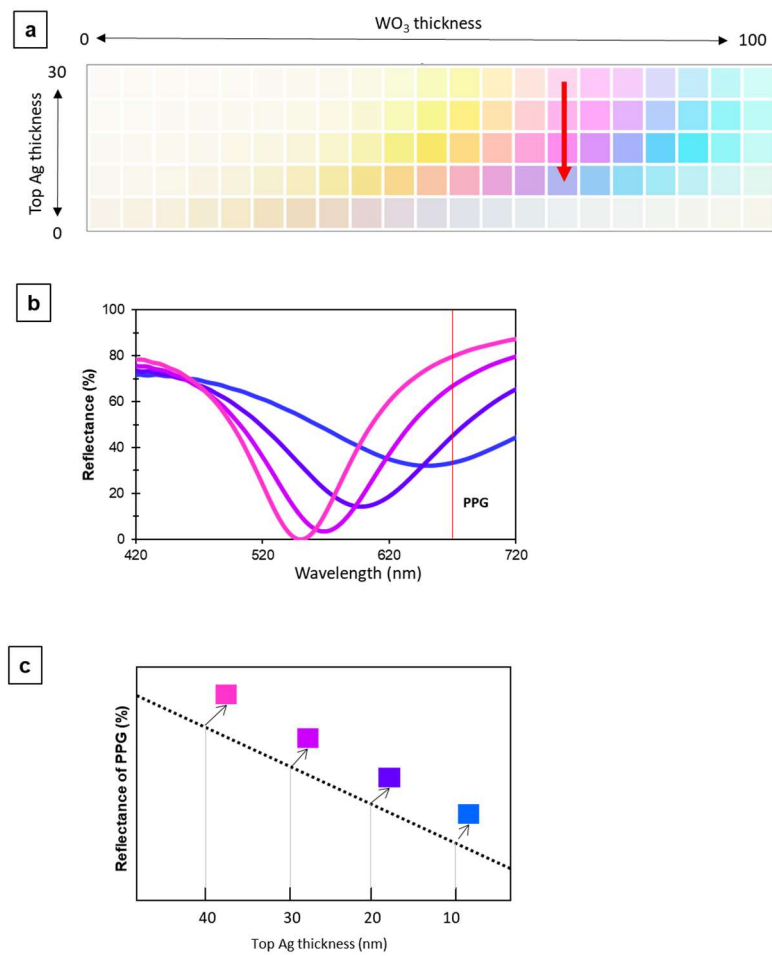
Figure 13 FDTD Analysis (a) Spectrum analysis and color map of NO₂ gas Sensor with top Ag thickness 0 ~ 30 nm and insulator WO₃ thickness 0~100 nm (b) Spectrum change of NO₂ gas sensor (c) reflectance change at 660 nm of NO₂ Sensor

3.3. Sensor Fabrication

The deposition of the FP-cavity structure was conducted using an e-beam evaporation system (Samhan Vacuum Tech. Co. Ltd., STM-100). To obtain a uniform film surface, the vacuum condition of the chamber was maintained under 3.0×10^{-6} Torr. As the substrate of the sensor, flexible polyethylene terephthalate (PET) was used, and sensors were fabricated with a mask manufactured using a three-dimensional (3D) printer. A 10 mm × 10 mm gas sensor was fabricated in a 5 × 5 array inside a 4" PET film. The deposition rate of the Ag layer was maintained at 1.0-1.5 Å/s. The deposition rate of the WO_3 layer was maintained at 0.3-0.5 Å/s (Table 1). The film thickness was monitored using a quartz crystal microbalance with angstrom-level sensitivity.

Figure 14a shows a photograph of the manufactured NO_2 colorimetric gas sensor. The blue region is the region of Ag-WO_3, and the purple region is the region of the colorimetric sensor having the Ag-WO_3-Ag layer. The spectrum of the prepared sample was examined using a spectrometer (Figure 14b). It exhibited a structural color with a peak near 550 nm, which is consistent with the design objective of visibility.

	Emission current	Evaporation Rate	Thickness	Tooling Factor
Ag	45 ~ 50 mA	1.0 ~ 1.5 Å s^{-1}	60 nm (lower) 40 nm (upper)	80%
WO$_3$	12 ~ 18 mA	0.3 ~ 0.4 Å s^{-1}	70 nm	100%
SiO$_2$ (Mask layer)	27 ~ 32 mA	1.5 ~ 2.0 Å s^{-1}	10 nm	85%

Table 1. E−beam evaporation condition of NO$_2$ gas sensor
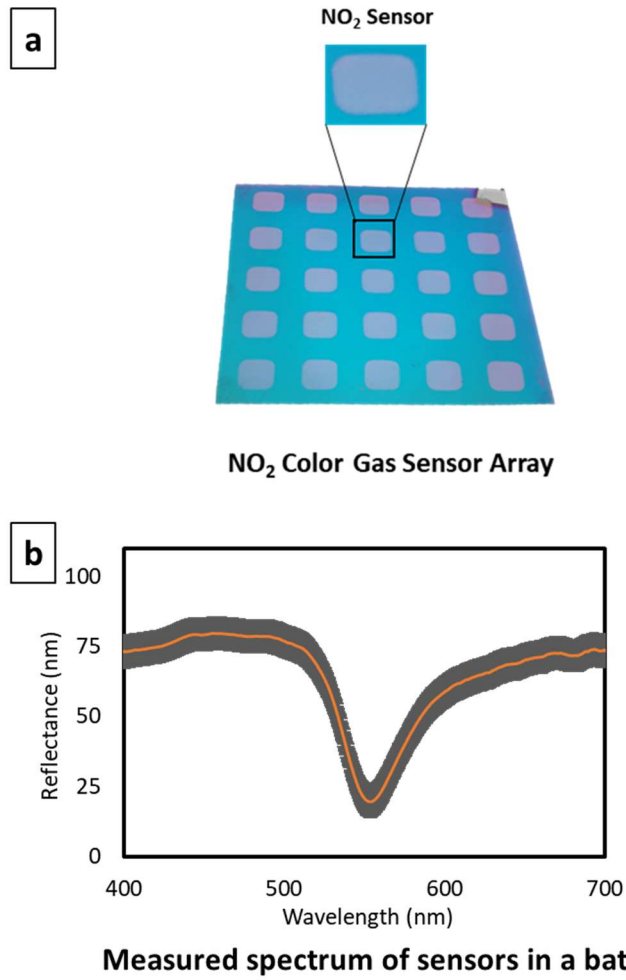
Figure 14 NO₂ colorimetric gas sensor fabrication (a) Image of fabricated colorimetric gas sensor array using 3D printed mask on PET substrate (b) Spectrum of Fabricated colorimetric gas sensor

3.4. Nonlinearity in manufacturing sensor

The nonlinearity of the manufacturing process should be considered to enhance the uniformity of the sensor. First, the thickness non-uniformity of the FB cavity can affect the initial value of the sensor. It is important to determine the optimal deposition conditions with a small variation in the deposition thickness by analyzing the process parameters.

Second, to ensure the uniformity of the sensor's sensitivity, the adhesion of the Ag layer must be considered. Factors affecting the adhesion uniformity are divided into three categories: process, surface, and temperature. In the e-beam process, the evaporation rate (R_m) changes as the target in the crucible receives energy from the electrons. The formula for the evaporation rate is as follows [34]:

$$R_m(T) \;=\; C\sqrt{\frac{M}{T}}\frac{P_e}{4r_0} \quad \text{------------------------------}(3{-}4)$$

Here, P_e is a function of temperature, and R_m can also be arranged as a function of temperature.

As R_m increases, the change in velocity that occurs when the deposited particles attach to the substrate increases, and the bonding force increases according to the formula for the changes in the amount of impact and momentum.

$$I \; = \; \Delta P \; = \; m\Delta v \; = \; m\Delta R_1 \text{ -----------------------}(3-4)$$

Therefore, we fabricated the sensor under three different evaporation rates (0.3, 1.0, and 2.0) and examined the nonlinearity according to the process. Sixteen samples were prepared for each condition, and a total of 44 samples were measured (4 defective samples were excluded). The center peaks of the sensors fabricated under the different deposition conditions had a standard deviation of 3.34 nm (Figure 15). An FDTD analysis indicated that the sensor's center wavelength was 547.94 nm, and the errors for the center wavelengths of the samples were -8.87, -2.52, and $+5.92$ nm. Thus, the evaporation rate of 1.0 Å/s is the desirable value for manufacturing with regard to the initial value of sensor (Table 2).

Regarding the thickness of the reaction layer, the sensor fabricated under the 1.0−Å/s condition had the smallest deviation of the stacking thickness (0.56 nm). Additionally, the deviation of the reflectivity among the 16 manufactured samples was the smallest (2.21%) at 1.0 Å/s. Therefore, considering only the initial state of the sample, the working condition of 1.0 Å/s is the most preferable.
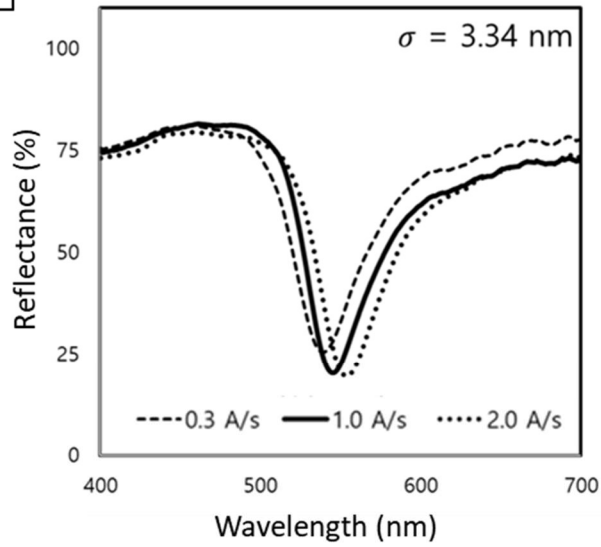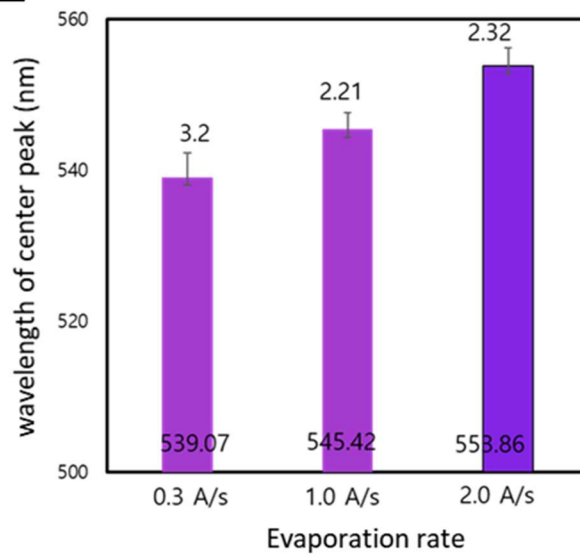
Figure 15 Spectral comparison of sensors with three different deposition rates

Evaporation condition	Evaporation rate (A/s)		
	0.3	1.0	2.0
Evaporation time (sec)	833	250	125
Peak error (vs FDTD) (nm)	−8.87	−2.52	+5.92
Thickness difference (nm)	+1.96	+0.56	−1.31
Deviation in a batch (%)	3.20	2.21	2.32

Table 2 Comparison of thickness uniformity according to three deposition conditions

Gas experiments was performed on the sensors manufactured under the three different conditions. Five sensors were tested under each condition, and a total of 14 samples were tested (1 contaminated sample was excluded). The sensitivity was evaluated according to the decrease in reflectance. Among the three conditions, the sensor fabricated under the 1.0 Å/s condition exhibited the largest decrease in reflectance (Figure 16).

The sensors fabricated at 2.0 Å/s had strong adhesion on the deposition surface owing to the high deposition rate, which led to a low reaction rate. The samples fabricated at 0.3 Å/s had lower reactivity than those fabricated at 1.0 Å/s, in contrast to our prediction. This appeared to be due to the increase in the binding energy caused by the change in the vacuum conditions and the radiant heat of the crucible arising from the long evaporation time. Among the fabrication conditions, the variation in the reaction rate was the largest for 0.3 Å/s (Table 3). Therefore, a deposition rate of 1.0 Å/s is the optimal process condition considering both the initial quality of the sensor and the reaction rate.
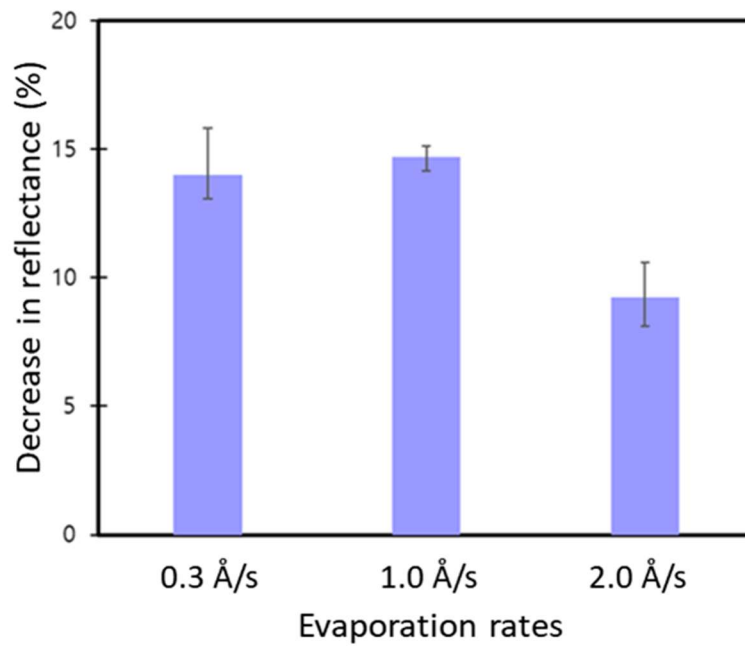
Figure 16 Gas experiment test for 3 evaporation rates （gas test
condition : 15 ~ 20 ppm , 22 ℃ and 5 hours）

Evaporation condition	Evaporation rate		
	0.3 Å/s	1.0 Å/s	2.0 Å/s
Number of samples	5	5	4
Reflectance change @ 660 nm	13.988	14.68	9.25
Standard deviation	1.08	0.366	1.03
Positive error	1.83	0.43	1.35
Negative error	0.93	0.55	1.14

Table 3 Comparison of sensing rate according to three deposition conditions

3.5. Setup for gas experiment

For the experiment, a gas chamber capable of fine-tuning the gas concentration was fabricated (Figure 16). A mass flow controller (MFC) was used to accurately control the amount of input gas. The MFC automatically controlled the flow of gas according to a set flow rate transmitted by an electrical signal and was not affected by changes in the operating conditions or gas pressure.

The sequence of the gas-sensor experiment was as follows. To prevent the reverse flow of the input gas, low vacuum conditions of 10^{-2} Torr were applied using a rotary pump. Next, NO_2 gas with the set concentration was injected using the MFC controller. The NO_2 input gas had a concentration of 300 ppm, and air was used as the balance gas. When NO_2 gas was injected into the chamber at the flow rate determined by the MFC controller, its pressure decreased to the atmospheric pressure level in 30 min, and its concentration was kept constant.

A commercial NO_2 gas sensor was used to confirm the concentration changes in real time. Two commercial sensors were used to obtain accurate results below 10 ppm. An Arduino-based NO_2 gas sensor (CJMCU-6814, NO_2 sensing range: 0.05–10 ppm)

was used under low-concentration experimental conditions of 0–10 ppm. Additionally, an NO_2 commercial sensor manufactured by ELT Sensor was used (NO_2–SM30–3V, NO_2 sensing range: 0.05–10 ppm). At concentrations above 10 ppm, the NO_2 gas concentration was measured using a commercial NOx sensor (UniNOx, Continental; accuracies of ±10% at 100–1500 ppm and ± 10 ppm at 0–100 ppm) and the measuring program Canoe developed by Vector.
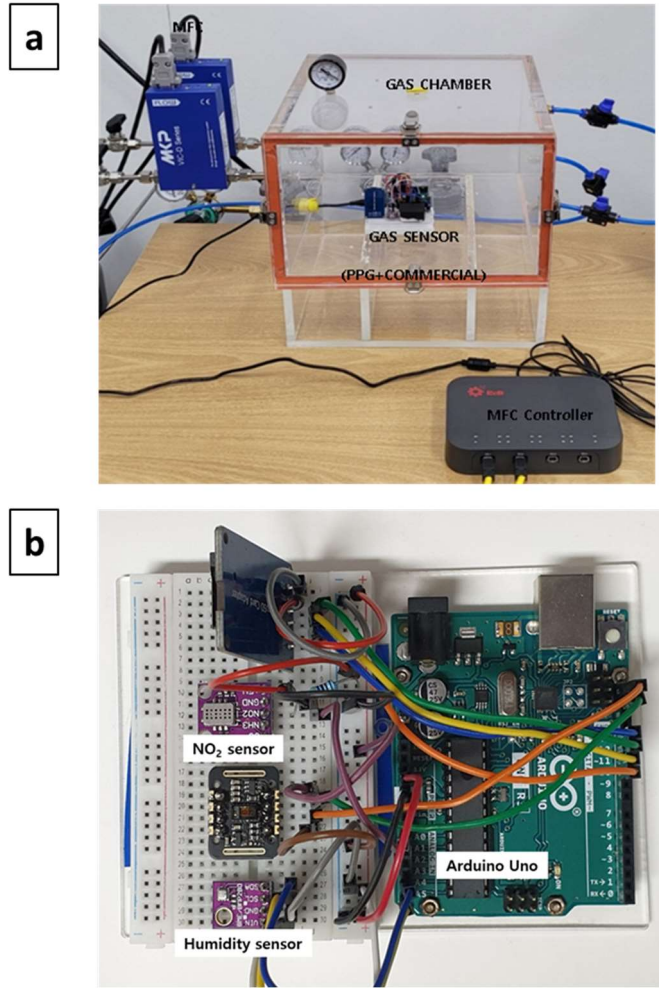
Figure 17 a. Setup for gas exposure experiment b. arduino based NO_2 gas sensor using CJMCU−6814

3.6. Results and discussion

Commercial corrosive gas sensors, including NOx gas sensors, operate at high temperatures and have limited applications owing to wearability and power-consumption issues. The proposed concept of a wireless color-based gas sensor extends the application range of gas sensors, including wearable devices. For the practical application of the colorimetric gas sensor, a flexible sensor was fabricated using PET film as a base material, and then the reaction rate was measured under conditions of room temperature and 1 atm. After exposure to 200-ppm NO_2 gas, the color gradually changed, and when the design including a masking layer was used, the color could be visually distinguished after 5 min of exposure. A spectral analysis was performed using a compact spectrometer (QP400-2-VIS-NIR; Ocean Optics/Ocean Insight). For reference, the standard white color of the Scinco ColorMate spectrophotometer (Scinco, Daejeon, Korea) was used. The results exhibited a similar trend to the FDTD analysis values shown in Figure 13b. The color-changing reaction ended in the blue light region (Figure 18).
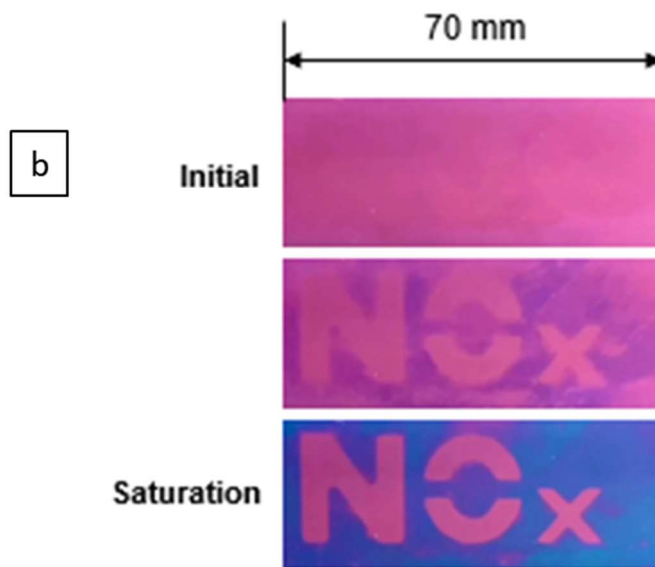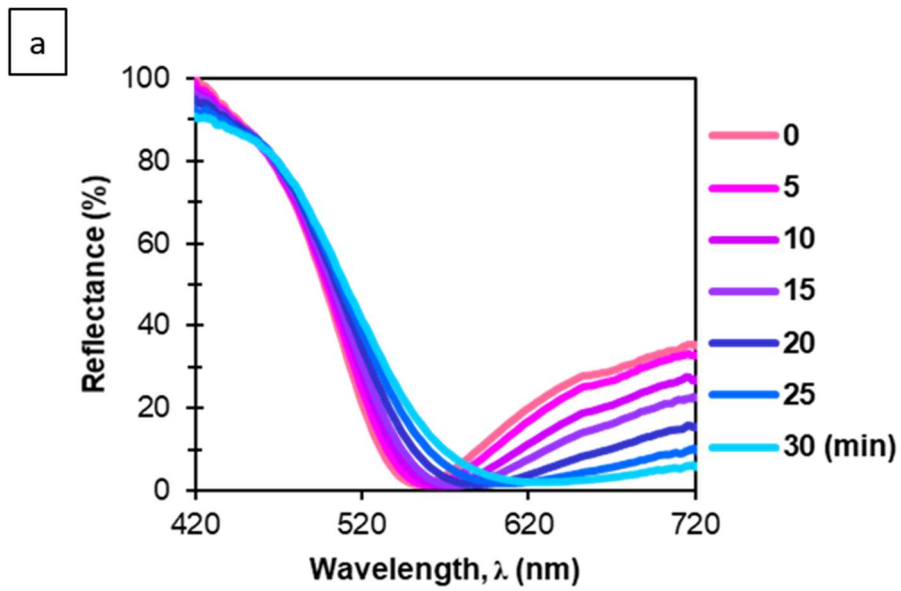
Figure 18 Toxic gas color detector using color change of NO_2 colorimetric gas sensor a. reflectance change of NO_2 sensor (200 ppm, in room temperature) b. image of color change of NO_2 sensor

3.7. Characterization of sensor

Figure 19 shows the cross section of the Ag–WO$_3$–Ag structure, which was examined using TEM. The thickness of the Ag–WO3–Ag structure before the change was measured as 25.03 nm–71.3 nm–16.76 nm. After exposure to NO$_2$ gas, residues were visible on the Ag surface, and the thickness of the Ag layer was reduced to 7–10 nm. The changed sample was exposed for 3 weeks in an NO$_2$ environment; thus, the Ag layer on the surface had a certain level of saturation.

Energy−dispersive X−ray spectroscopy (EDS) was performed to analyze the residue related to the corrosion reaction of Ag, but N and O were not detected on the surface. We confirmed that the Ag−layer corrosion reaction is a corrosion reaction that does not leave nitrogen oxide on the surface. Additionally, N was not found even inside the nano−thin film. Thus, there was no diffusion inside the film, e.g., SiO$_2$, and the reaction rate can be analyzed using the rate equation rather than the diffusion theory.
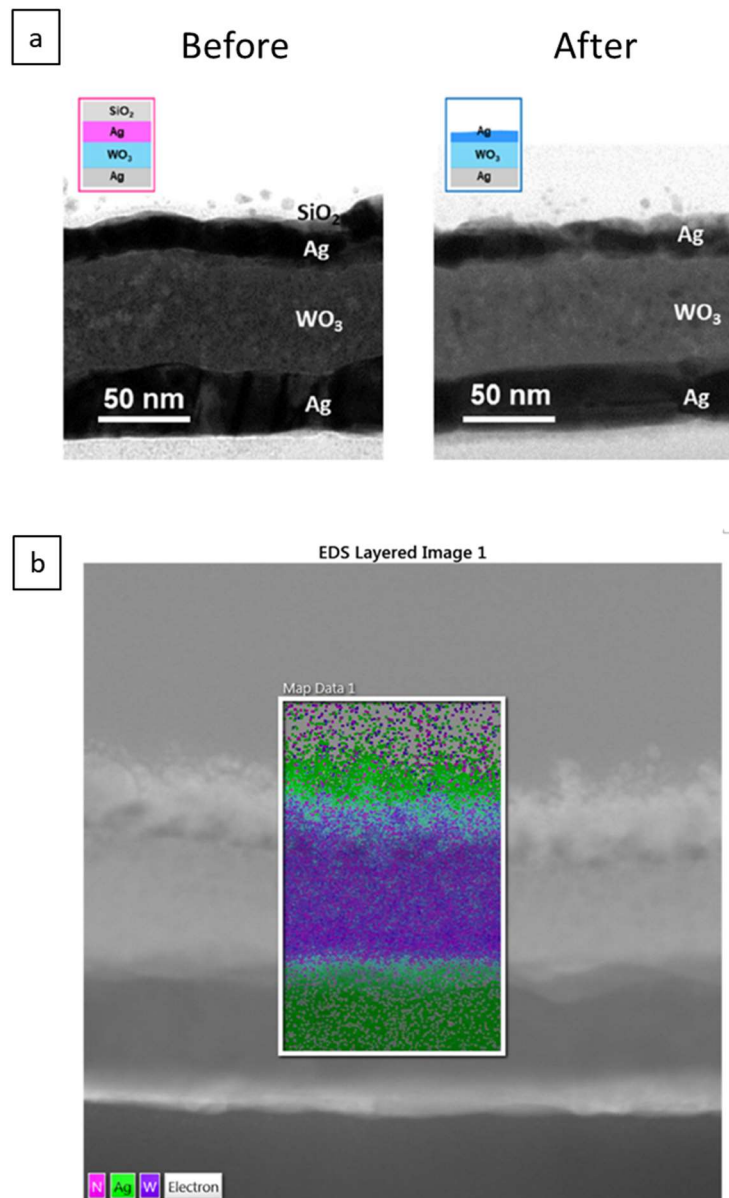
Figure 19 Characterization of NO₂ colorimetric gas sensor (a) the section image of Colorimetric sensor before reaction with NO₂ (FIB.TEM.) (b) Material property analysis using EDS (Energy Dispersive X-ray Spectroscopy)

To confirm the sensitivity of the sensor according to the gas concentration, a concentration experiment was conducted using NO_2 gas. In the experiment, concentrations of 50, 100, and 200 ppm were tested. The reaction time was shortened as the concentration increased, and the final color of the sensor was light blue at all the concentrations. According to the experimental results, the relationship between the concentration (x) and the inverse of the reaction time (y) was investigated, as shown in Figure 20b.

$$y = -9 * 10^{-8}x^{3.1144}$$ ----------------------------(3-5)

On the basis of the analysis, the reaction rate of the gas sensor according to the NO_2 gas concentration was explained by the rate equation of the gas reaction.

To verify the reactivity of the sensor according to the temperature, the experiment of NO_2 gas was performed at different temperatures. The reaction time was shortened as the temperature increased, and the final color of the sensor was light blue at all the temperatures. According to the experimental results, the relationship between the temperature (x) and the natural logarithm of the rate constant, i.e., the inverse of the reaction time (y), was investigated, as shown in Figure 20b.

$$y = 0.0061x + 1.7638 \quad \text{-----------------------}(3{-}5)$$

$$(R^2 = 0.9975)$$

Using this property, we can appropriately adjust the reaction rate and sensitivity of the proposed sensor by controlling the temperature of the sensor according to the application.
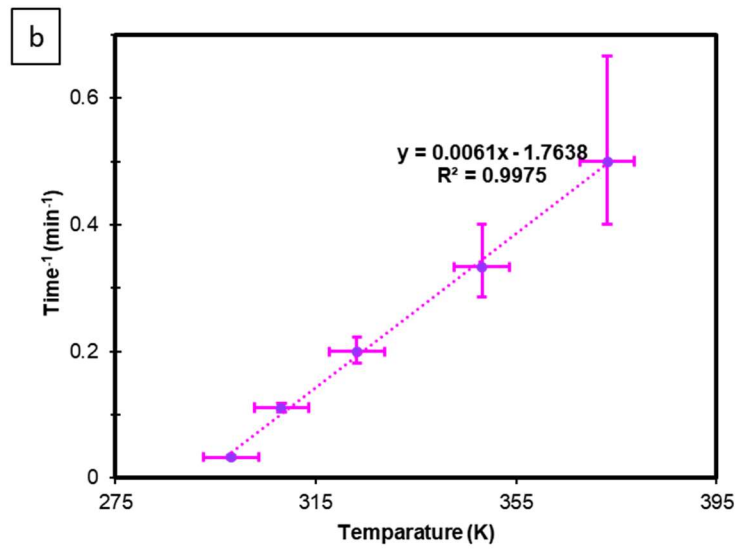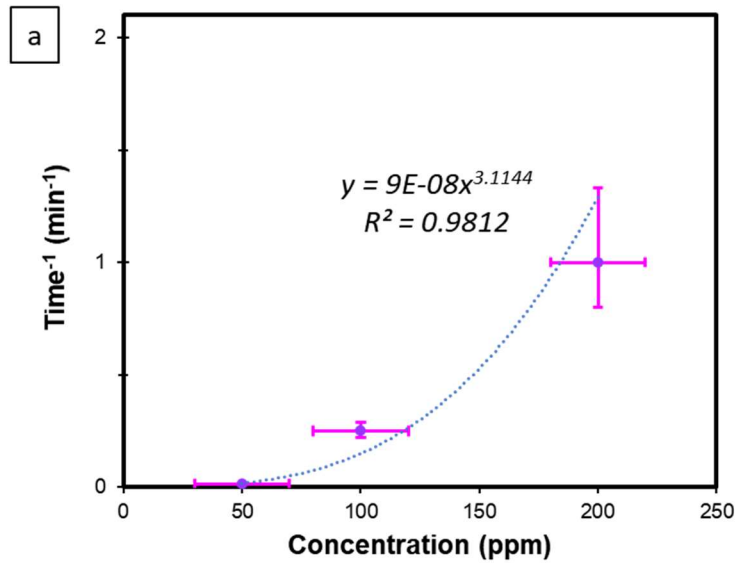
Figure 20 Reflectance change of NO_2 colorimetric gas sensor according (a) the correlation between concentration and time (b) the correlation between temperature and time

3.8. Environment and reliability test

The developed NO_2 gas sensor is composed of an Ag thin film on the exposed surface. The Ag thin film can be easily corroded under high-humidity conditions; thus, it is important to manage the quality of the sensor. Therefore, an environmental-resistance test of the developed sensor was conducted. With exposure to an environment of 75% humidity at room temperature for 48 h, performance degradation occurred at 450 nm and 520 nm or less, but the center peak remained constant (Figure 21a).

A gas-sensor module was manufactured for environmental testing under severe humidity (Figure 21b). A GoretexR membrane was attached to the inlet and outlet of the sensor. GoretexR is a F-coated fabric material that prevents the penetration of water droplets with sizes of <100 μm and suppresses the ingress of excessive water vapor. When the gas sensor was tested in the module state, there was no problem for 48 h at 40℃ and 95% humidity (Figure 21c).

Additionally, we conducted a 5095 test, which is the industry standard for high-temperature (50℃), high-humidity (95% relative humidity (RH)) testing. This test can be used to quickly check the durability of a product and to determine the distribution environment by conducting a test harsher than the actual environment. The manufactured NO_2 sensor unit had a durability of 12 h according to the 5095 tests, and the module with the membrane exhibited a durability of 24 h. This is classified as a failure according to industry standards, and durability improvement is required for practical application of electronic products.

However, in an experiment in the module state, the flow rate of the gas decreased, and the reaction rate of the sensor also decreased. Therefore, it is recommended that this sensor be used as a single sensor without a membrane and be used as a disposable sensor that is discarded after use.
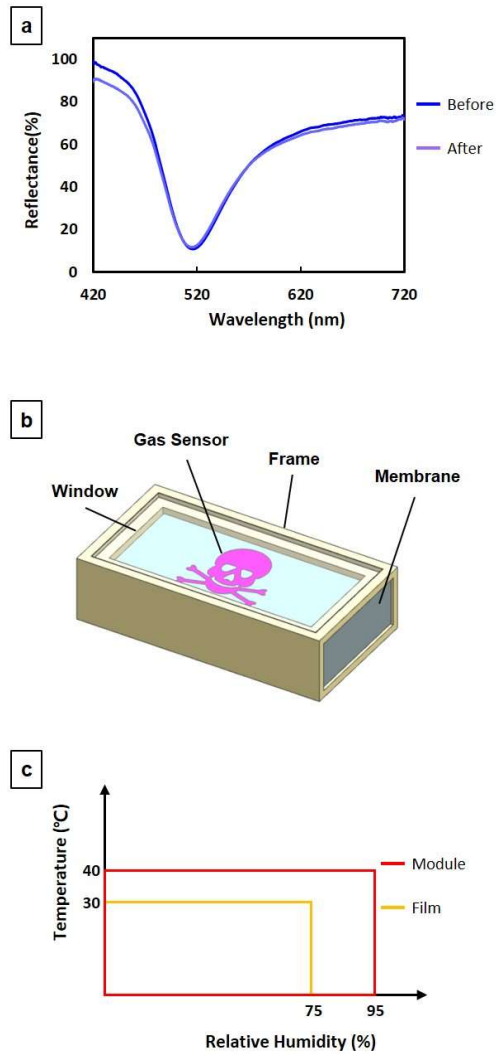
Figure 21. Results of environment resistance test. (a) No change before and after constant temperature and humidity test result (303K 75%) (b) Fabrication of sensor module with improved moisture resistance using membrane (c) Results of improving environmental resistance of colorimetric gas sensors using module design (30℃ 75% → 40℃ 95%)

3.9. Sensitivity tuning using micro patterning

We tested the developed NO$_2$ colorimetric sensor in a high-concentration environment of 50 – 200 ppm. U.S. industrial environment standards warn workers in hazardous areas that exposure to a maximum concentration of $\geq$35 ppm for 5 min is dangerous. Therefore, for industrial safety, the sensor should be able to detect low concentrations (<35 ppm) of NO$_2$.

Thus, we attempted to improve the sensing performance by securing the surface area through micropatterning. Figure 21 shows a micro-patterned sample fabricated through FIB machining and laser machining. FIB is an ultra-precision process capable of sub-microscale machining. The sensor fabricated with a pattern width of 1 μm using FIB had a structural color owing to the micro-pattern, and the 20-nm-thick Ag layer in the upper layer was removed; thus, it did not play the role of an NO$_2$ gas sensor. The minimum processing depth of FIB exceeded 25 nm; thus, it was not suitable for fabricating the NO$_2$ sensor.

A $100-\mu$m-level pattern was processed using a laser. It was possible to tune the peak shift and the change in reflectance in some sections by changing the laser power and the pattern geometry. There was no significant performance change of the sensor in the processing at the scale of several hundred micrometers. However, it is expected that the sensitivity can be improved through pattern optimization.
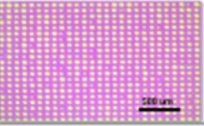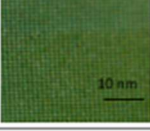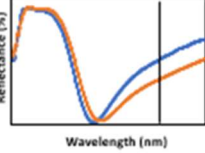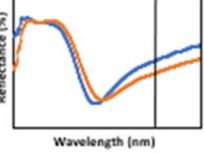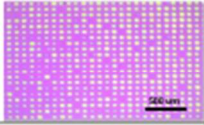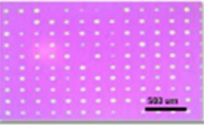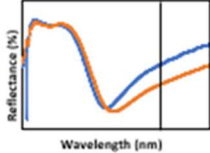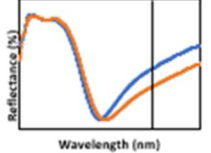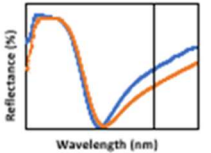
	No Patterning	Laser energy	Pattern width
Laser	FIB	-	20 mW
Pattern	1 µm	-	100 µm
Before			
After			
R Change @ 660	-	16.65	10.38
Peak shift	-	10.7	11.751
Spectrum Change	-		

	Pattern width		
Laser	15 mW		
Pattern	100 µm	200 µm	300 µm
Before			
After			
R Change @ 660	**16.49**	14.64	14.08
Peak shift	**11.733**	8.9	8.558
Spectrum Change			

Table 4. Results of micro patterned NO$_2$ gas sensor test

Chapter 4. Measurement and data processing

4.1. Monochromic analysis

For measuring physical quantities, colorimetric sensors have the advantages of simple measurement and no need for additional measurement systems. However, color perception using human cone cells is not proportional to the wavelength. Humans are sensitive to color in the range of 500 – 600 nm; thus, quantitative measurement is difficult.

Quantitative measurements can be performed using spectrometers. Although full–spectrum analysis can be performed using spectrometers, they are expensive and large and have many points to manage, such as the light reference and light source. Therefore, by using monochromatic analysis, quantitative measurements can be performed with a simpler device.

Figure 22 shows the FDTD analysis and experimental values of the reflectance change of the NO_2 gas sensor at a wavelength of 660 nm. According to the FDTD analysis, as the thickness of the upper Ag layer, which was the reactive layer for NO_2 gas, decreased at 25 nm, the reflectance decreased linearly ($R^2 = 0.98$).

In the NO_2 experiment, the reflectance decreased linearly as the exposure time to NO_2 gas increased, and its trend was similar to that in the FDTD analysis. Thus, the developed NO_2 gas sensor can measure the actual cumulative gas exposure via single−wavelength observation (660 nm).
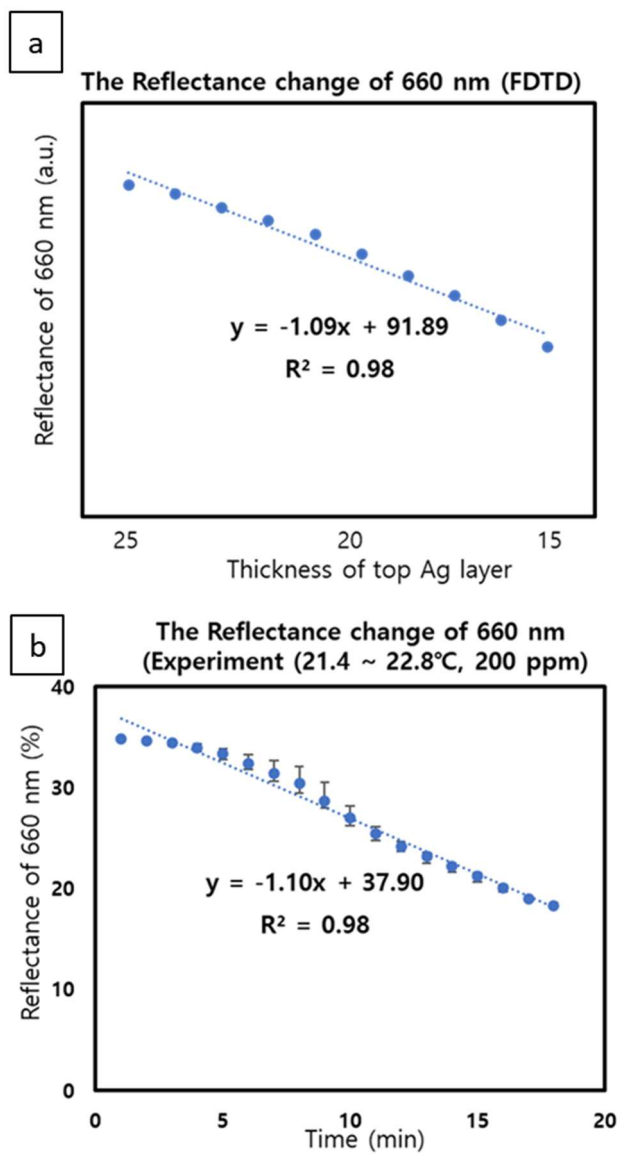
Figure 22. Results of monochromic analysis at 660 nm (a)FDTD
analysis (b) results of NO₂ gas experiment (200 ppm, RT)

4.2. Combination of PPG sensor and colorimetric sensor

For monochromatic analysis of the colorimetric gas sensor, we used a PPG sensor [35]. PPG sensors are mainly used to detect changes in blood flow in wearable devices such as smart watches. As shown in Figure 23a, a PPG sensor consists of a light-emitting part composed of an LED and a receptor that detects reflected light and has low power consumption of <1 mW. In this study, a MAX 30102 PPG sensor was used for connection with Arduino. Using this sensor, the NO_2 gas concentration was calculated by changing the reflectance value at a single wavelength of 660 nm instead of measuring the entire spectrum (Figure 23c).

Table 5 presents the specifications of the PPG sensor used in this study. The measurement wavelength range was 650 – 670 nm, and the accuracy was 0.05% based on the full scale. The operating temperature ranged from −40 to +85℃, and the repeatability was measured to be 0.004%–0.015% based on the full scale depending on the color. The measured repeatability was relatively high, making the sensor unsuitable for ultraprecision measurements.

60
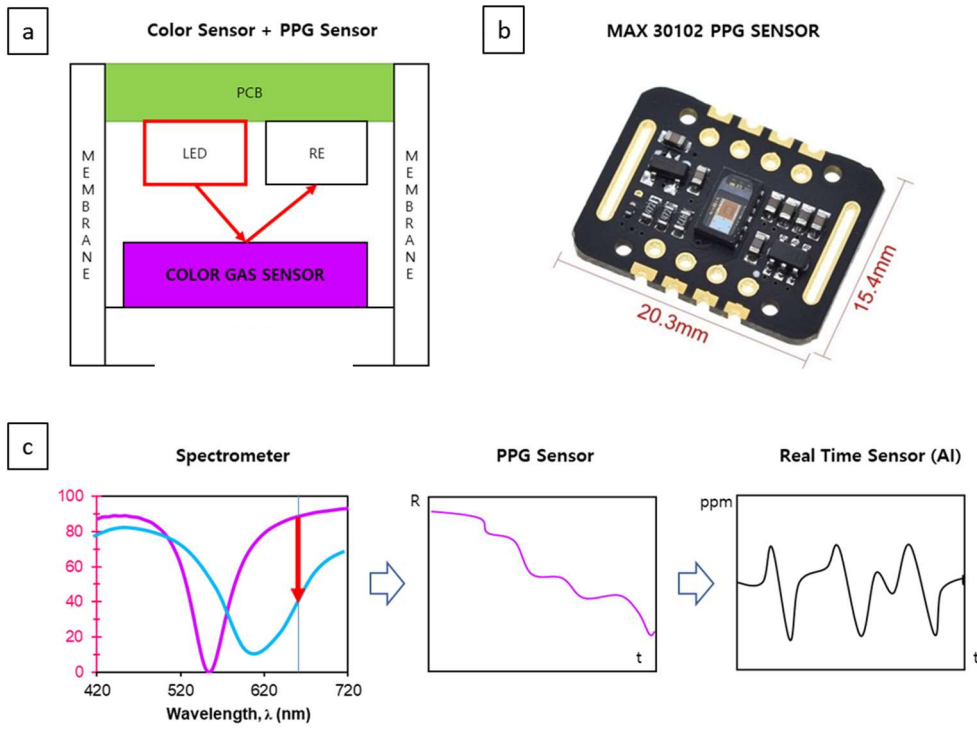
Figure 23. The combination of colorimetric gas sensor and PPG sensor (a) The gas sensor structure using PPG sensor and membrane (b) MAX 30102 PPG sensor for Arduino uno (c) The schematics of real time gas sensing using PPG sensor and AI

parameter	Value (min-typ-max)			units
Wavelength	650	660	670	nm
Accuracy		0.05		% of FS (Full Scale)
Operating Temp	-40	~	+85	Degree Celsius
Repeatability	2.79	~	10.34	PPG value
	0.004	~	0.015	% of FS (Full Scale)

Table 5 The specification of PPG sensor (MAX 30102)

4.3. AI based regression and calibration

By combining the colorimetric gas sensor and the PPG sensor, we obtained a quantified signal in the form of an integer for the reflectivity value changed by exposure to NO_2 gas. AI-based regression was used to improve the reliability of the sensor. The PPG sensor used can receive PPG (reflectance of 660 nm) values, irPPG (reflectance of 880 nm) values, and temperature data, and a low-power humidity sensor was added.

The PPG sensor value is not completely linear, but the linearity can be compensated by receiving the PPG + irPPG value together. The monochromatic LED, which is the light-emitting part of the PPG sensor, is affected by the temperature, and the error of the light-emitting part can be compensated by the temperature sensor. The Ag corrosion reaction caused by NO_2 gas is the dominant reaction of the colorimetric gas sensor, and the effect of H_2O on the reaction rate can also be considered through humidity measurements. Figure 24 shows a regression algorithm using a recurrent neural network (RNN).
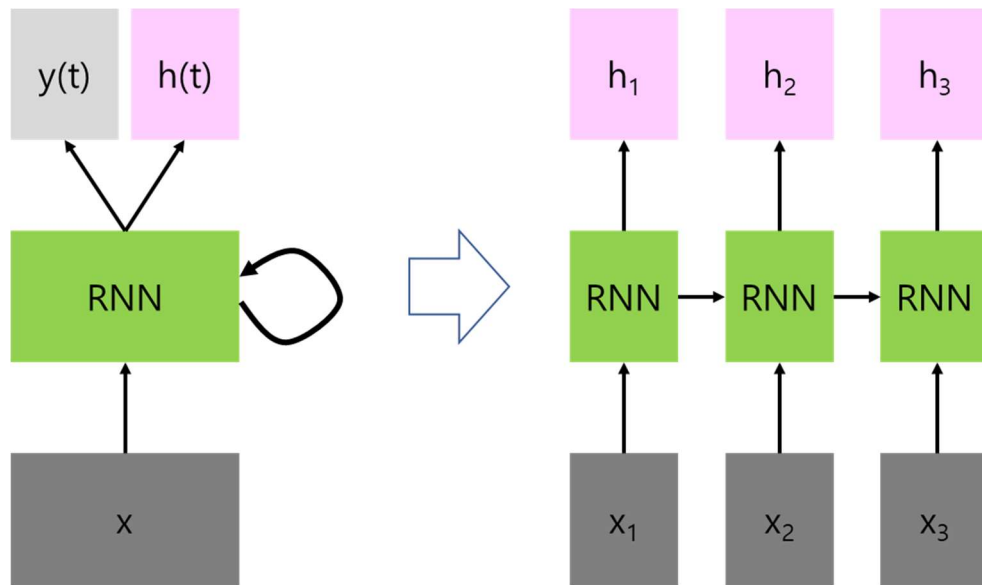
Figure 24. Regression Algorithm based on RNN

4.4. AI algorithm (LSTM)

The RNN is an artificial neural network-based algorithm that has recently attracted attention along with convolutional neural networks. In the RNN, hidden nodes are connected to form a directed cycle, which is suitable for sequentially appearing data such as voice and text (Figure 24).

The LSTM model is a type of RNN that connects nodes in a temporal sequence to represent the temporal dynamic behavior. Compared with the simple RNN model, LSTM achieves outstanding performance by overcoming exploding and vanishing gradient problems [36].

Because the NO_2 gas-sensing mechanism is a reaction to the accumulation of corrosion caused by the NO_2 gas, the RNN is a reasonable solution to include the corrosion history. In addition, because the initial state affects the corrosion pattern, LSTM is selected to reduce the vanishing gradient problem. Figure 25 shows a schema of our algorithm with LSTM layers. To predict the gas concentration using the proposed sensor, PPG, IR-PPG, temperature, and humidity data were used.
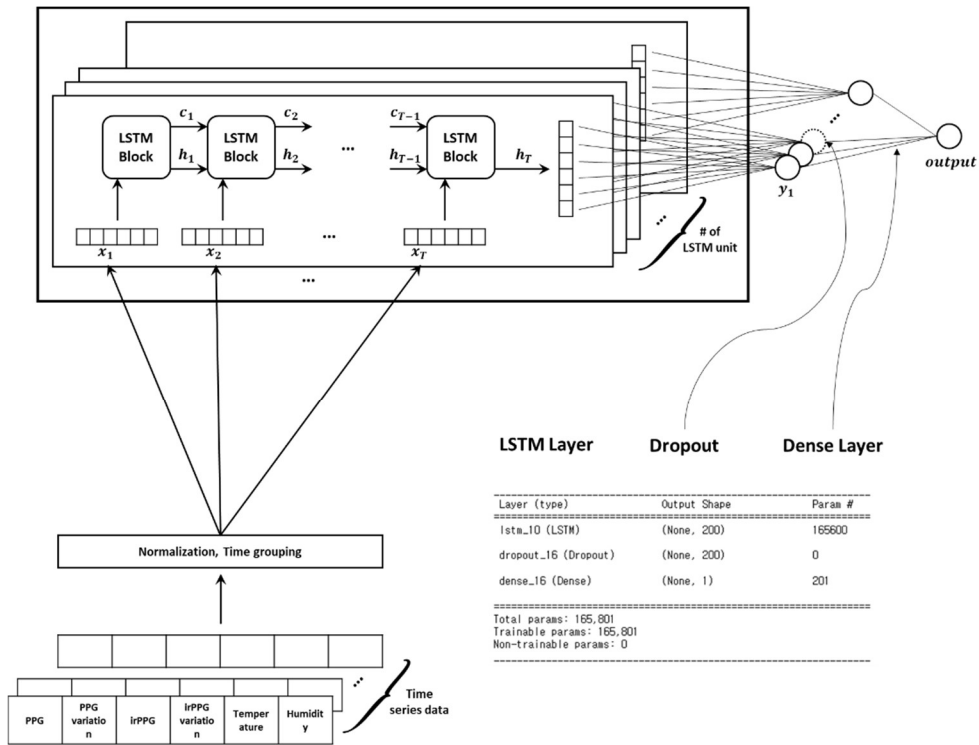
Figure 25. The schematic of LSTM

As previously mentioned, because the reflectance of the proposed sensor depends on the amount of corrosion, PPG and IR-PPG values are used to measure the reflectance variation. The PPG value represents the reflectance in the 660-nm region to a 16-bit number, and the IR-PPG value represents that in the 880-nm region. Additionally, the temperature was collected because the amount of light emitted by a monochromatic LED depends on the temperature. Regarding humidity, as indicated by Equations (3-1) and (3-2), in the corrosion reaction of NO_2 gas, the amount of moisture in the air affects the reaction rate. It was added to the input layer to include the effect of humidity on the corrosion reaction. Finally, the PPG and IR-PPG variations were calculated and added to the input layer.

These six-dimensional data were normalized with the z-score to fit most of the data in the specific range, for example, 0 ℃ was converted to -2.5, and 100 ℃ was converted to 2.5. To make the collected data suitable for LSTM, we grouped them into time intervals. After this preprocessing, the data were input for model training. During the training, a dropout layer was used between the LSTM layer and the dense layer to prevent overfitting [37].

For improving the performance of our AI model, data preprocessing was essential. Considering the working conditions of the proposed sensor, we set the temperature range as 0–100 ℃ and

the humidity range as 0%–100%. We normalized the collected data to the z–score with this range, preventing serious error when out–of–range data were input. Similarly, the PPG and IR–PPG data were normalized. The hyperparameters of the model also affect the performance. We set the sample length as 40. Because the data time interval was approximately 7.5 s, 40 means one dataset contains 5 min of data, and it is our target time to alarm hazardous gas to user. We set a LSTM unit to 200, and the model achieved adequate performance while minimizing the number of the parameters. In the training process, we used the "HeUniform" initializer and the "L2 norm" regularizer to prevent overfitting.

Figure 26 shows the measured data and training data for our model. For the test set in Figure 27, the standard deviation of the error was 1.34 ppm.
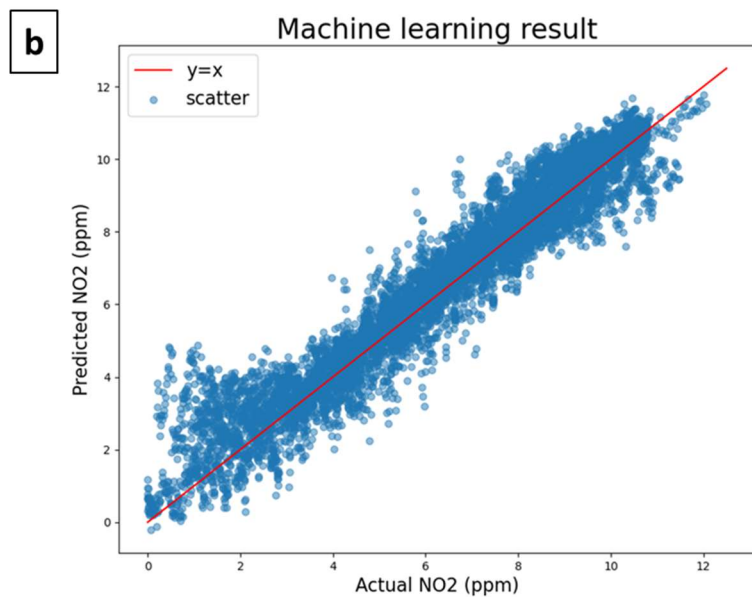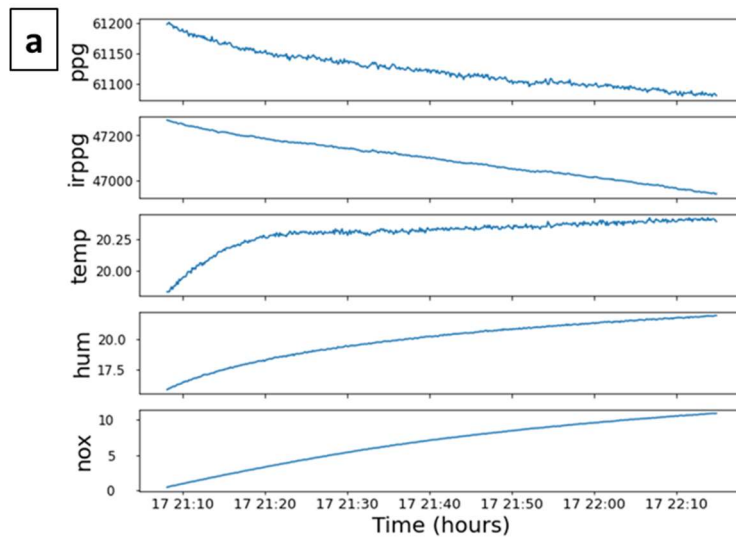
Figure 26. a. The back data of NO₂ gas experiment in setup b. training data of LSTM
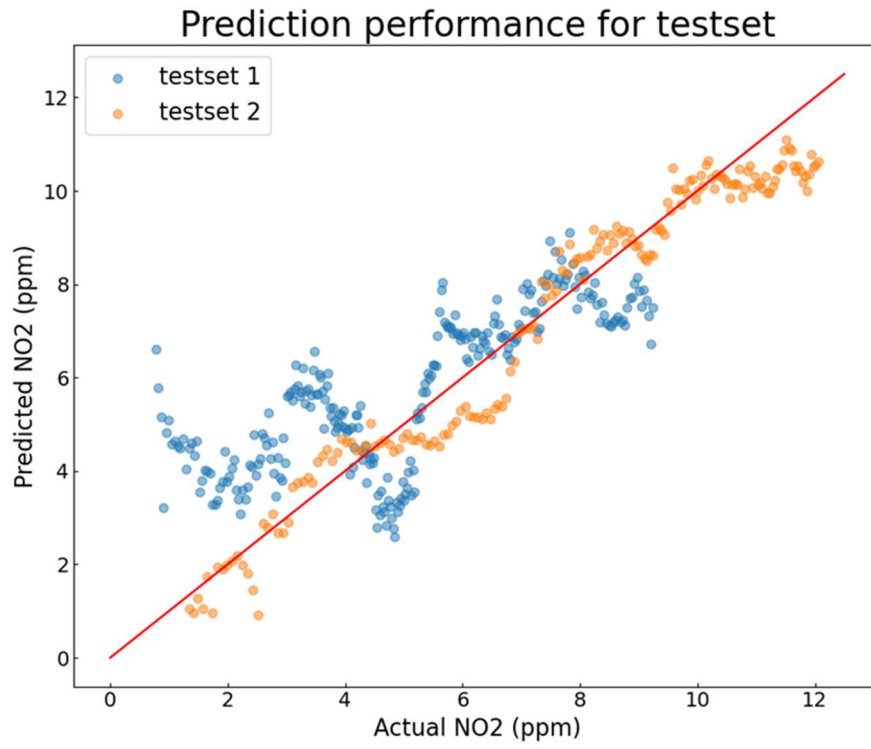
Figure 27. The test results of LSTM

4.5. Real-time gas monitoring using IoT

Most commercial harmful-gas sensors have the problem that the use time of the wearable device or mobile device is limited by the high operating temperature and power consumption. This makes continuous monitoring, which is the most important requirement for hazardous-gas monitoring, difficult. In this study, harmful gases could be detected with a low power through the combination of the gas sensor and the PPG sensor, and it was changed to a real-time signal through AI. To enable continuous monitoring, a low-power design should be used for the HW of the wearable device.

We proposed a watch-type wearable device and HW LOGIC that can reduce the power consumption (Figure 28). The most significant sources of power consumption in wearable devices are the LCD, SPK, and WIFI communication devices. We selectively activate power-hungry operations in certain situations. If the power is turned on using the slide key on the side of the device, only the gas sensor operates under 3 ppm, i.e., the US safety standard for NO_2 gas, and the LCD and WIFI devices are turned off. The SPK and LCD devices operate at 3-5 ppm, which is the warning standard for long-term workers. In the SPK device, a low-volume alarm sounds, and the

LCD displays "WARNING." Above 5 ppm, which is the warning standard for short-term workers, the maximum volume alarm sounds at SPK, and the LCD displays the phrase "DANGER". Through this circuit, it shows the use time that can be used for up to 5 d or more at the NO_2 concentration in the normal state.
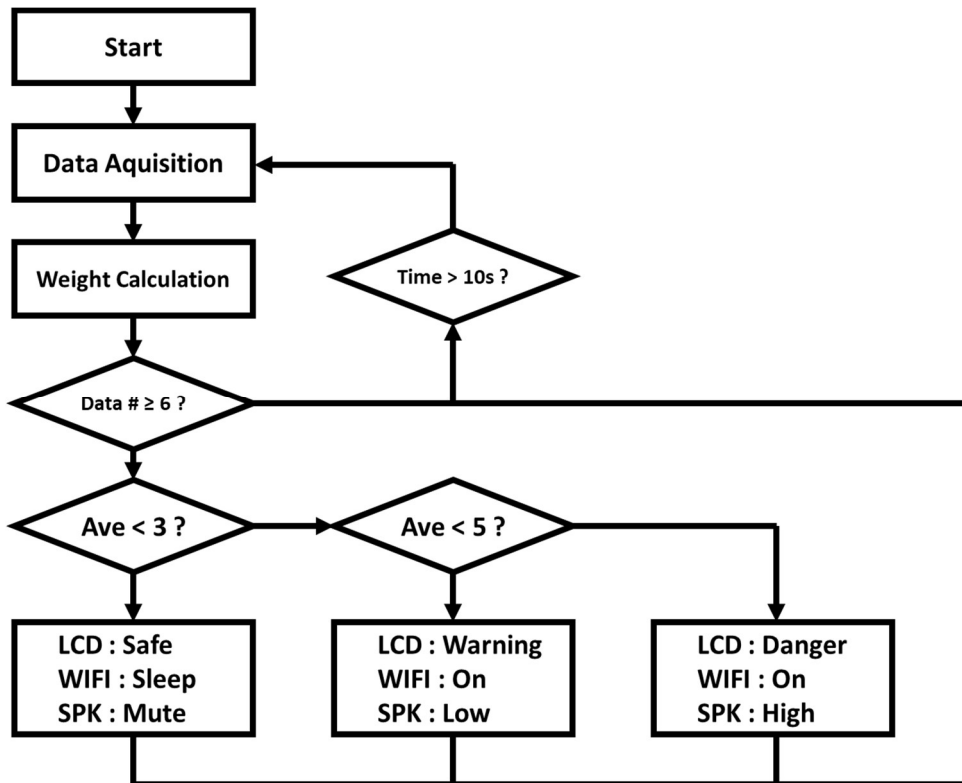
Figure 28. Logic of real−time gas monitoring using IoT

Chapter 5. Application

5.1. Smart factory gas monitoring system

Nitrogen oxide is a harmful gas generated in various industrial sites, e.g., cement manufacturing and fossil-fuel combustion. As cleaning workers have recently died from exposure to NO_2 gas, the detection of nitrogen oxides is important [10].

Industrial environment safety is a crucial field for smart factories. Figure 29 shows the operation scenario of the real-time hazardous-gas detection system in a smart-factory environment. When the installed gas-sensor module detects harmful gas, the large-area colorimetric gas sensor indicates a dangerous situation by changing color. In addition, the module comprising the colorimetric gas sensor and PPG sensor quantifies the gas exposure and transmits this value to the cloud in real time through WIFI-based wireless communication. The server of the monitoring system acquires the data in real time and sends a feedback signal to the site if the gas concentration is above a certain level.
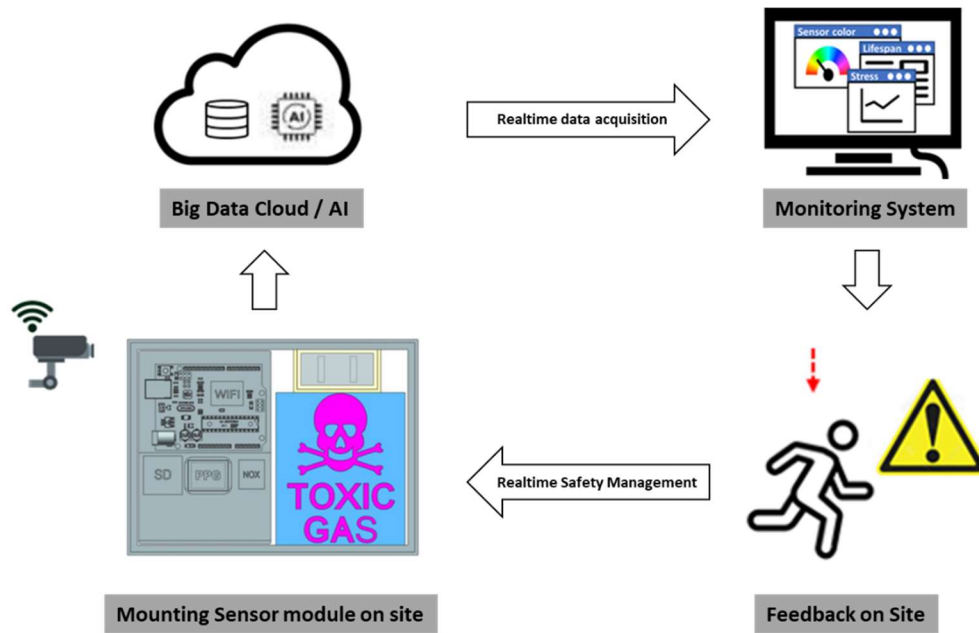
Figure 29. The schematics of smart factory using real time toxic gas monitoring system

We constructed a real-time gas monitoring system based on Arduino Uno. Figure 30 shows the manufactured gas-monitoring system prototype. For the colorimetric gas sensor, the MIM layer of the Ag-WO$_3$-Ag three-layer structure was deposited, and the PET film was cut with a laser to fabricate a mask. By covering the MIM layered area with a mask, SiO$_2$ was selectively deposited. Thus, when Ag and NO$_2$ caused corrosion, a warning message in the shape of a skull appeared.

In the reference colorimetric sensor in the package, a GoretexR membrane was attached to both sides, and an environmental test of the gas sensor was conducted. As the main printed circuit board (PCB), Arduino Uno WEMOS D1 R1 (an Arduino model that supports WIFI) was used, and the detected signal could be transmitted through WIFI in real time.

For comparison, MICS 6814 (a commercial electrical sensor that can be connected to Arduino) was also tested. The manufactured colorimetric gas sensor was connected to the PPG sensor (MAX30102). In preparation for failure of the WIFI wireless communication, a separate SD card socket was installed, and the data were backed up.

76
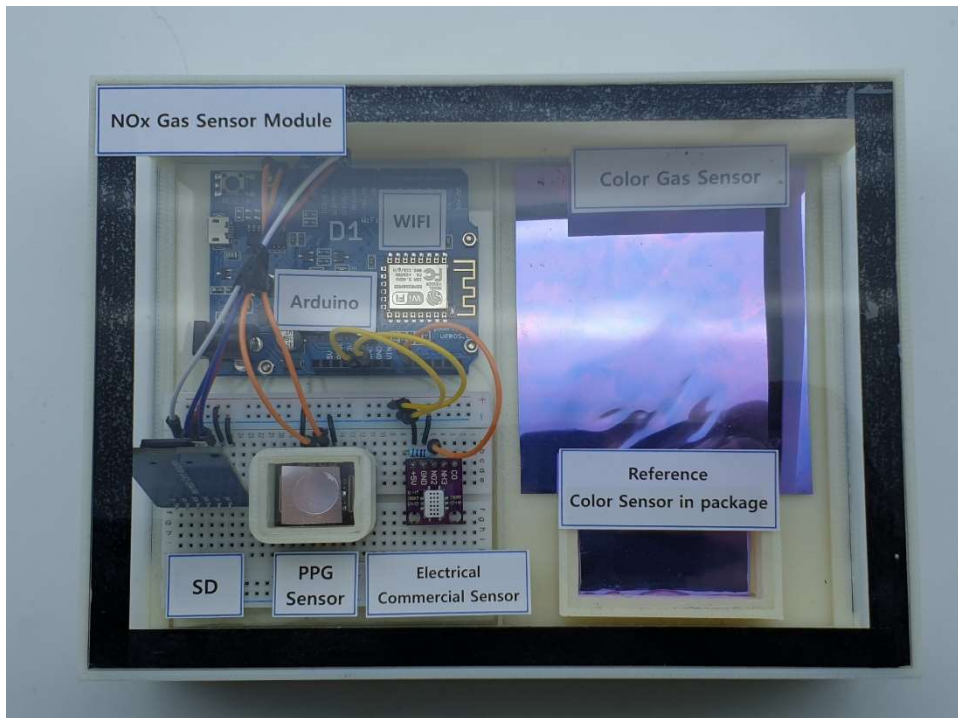
Figure 30. Real−time toxic gas monitoring system

The manufactured harmful-gas detection module was installed at a manufacturing industry site (Siheung-si, Gyeonggi-do, Global Concepts Korea). The installed site was one where a large amount of flame was generated, because the company manufactures automobile parts through the aluminum diecasting process.

Figure 31a shows the gas-sensor kit installed at the diecasting site. The installation location was selected such that operators could see while working, and the sensor distance was equal to the distance between the crucible and the operator. A total of four kits were installed, and monitoring was performed in real time, as shown in Figure 31b. The NO_2 gas concentration was measured to be 0.1–0.2 ppm on average. To accumulate learning data, 11 datasets were acquired over 6 months.
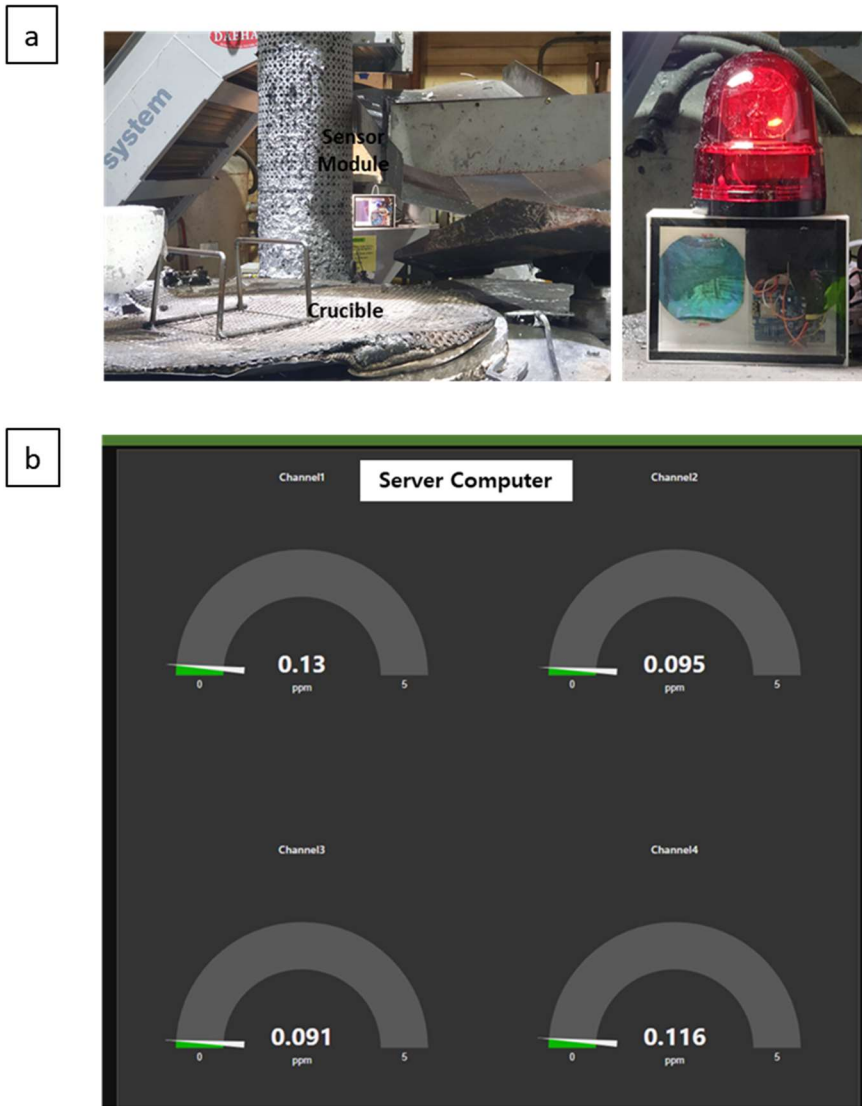
Figure 31. NO₂ gas sensing test in the diecasting manufacturing site

(a) Installment on the side of diecasting crucible (b) gas sensing data

on the server computer

Figure 32a shows the reflectance changes of the commercial NO$_2$ sensor and the PPG gas sensor. The sensors exhibited similar trends. The severe noise of the commercial NO$_2$ sensor based on electrical signals is caused by the high power consumption when the electrical signal at the diecasting site drives the crucible.

Figure 32b shows a comparison between the commercial gas sensor value and the value measured by the PPG sensor. The predicted NO$_2$ value was obtained by normalizing the change in the PPG sensor value, and a linear regression with the actual NO$_2$ value was performed. The correlation between the PPG sensor and the colorimetric gas sensor was strong, and it was confirmed that the developed system can be used in the field.
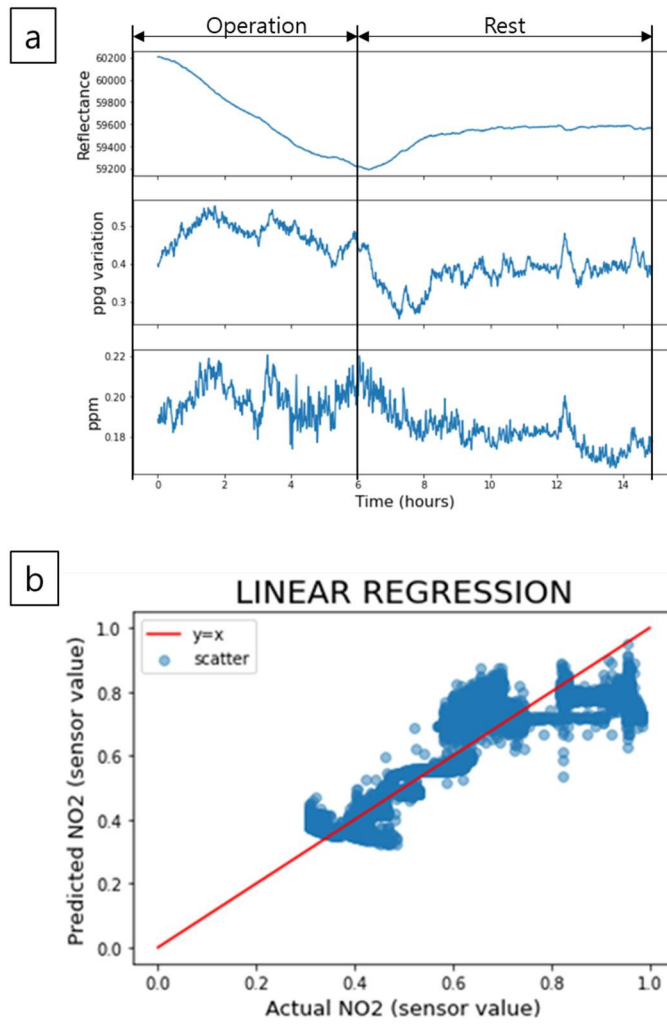
Figure 32. Gas sensor data calibration with commercial sensor (a) PPG sensor value vs commercial sensor (b) Linear regression data PPG sensor vs commercial gas sensor

5.2. Wearable gas monitoring system

Figure 33a shows a wearable device capable of real-time monitoring of harmful gases manufactured using the developed sensor and the derived algorithm. The watch-type wearable device had a tray structure into which a colorimetric gas sensor could be inserted from the outside. This made it possible to replace irreversible sensors and compensated for the short lifespan of sensors that react on the surface. To implement a continuous monitoring system, a switching circuit that can reduce the power consumption was implemented.

Figure 33b shows the design of the HW circuit. A 160-mmAh lithium-ion battery was mounted inside. A speaker that provided a warning (buzzer sound) under exposure to harmful gas was mounted, and the combination of the PPG sensor and colorimetric gas sensor detected noxious gas. An LCD was mounted for the display, and an Arduino Mini was used as a PCB. The slide key operation is shown on the right side of Figure 32b. It is composed of three stages (off, sensing, display and WIFI) and operates according to the exposure to harmful gases. In accordance with this configuration, a circuit capable of continuous gas detection for ≥ 72 h was implemented (Table 6).
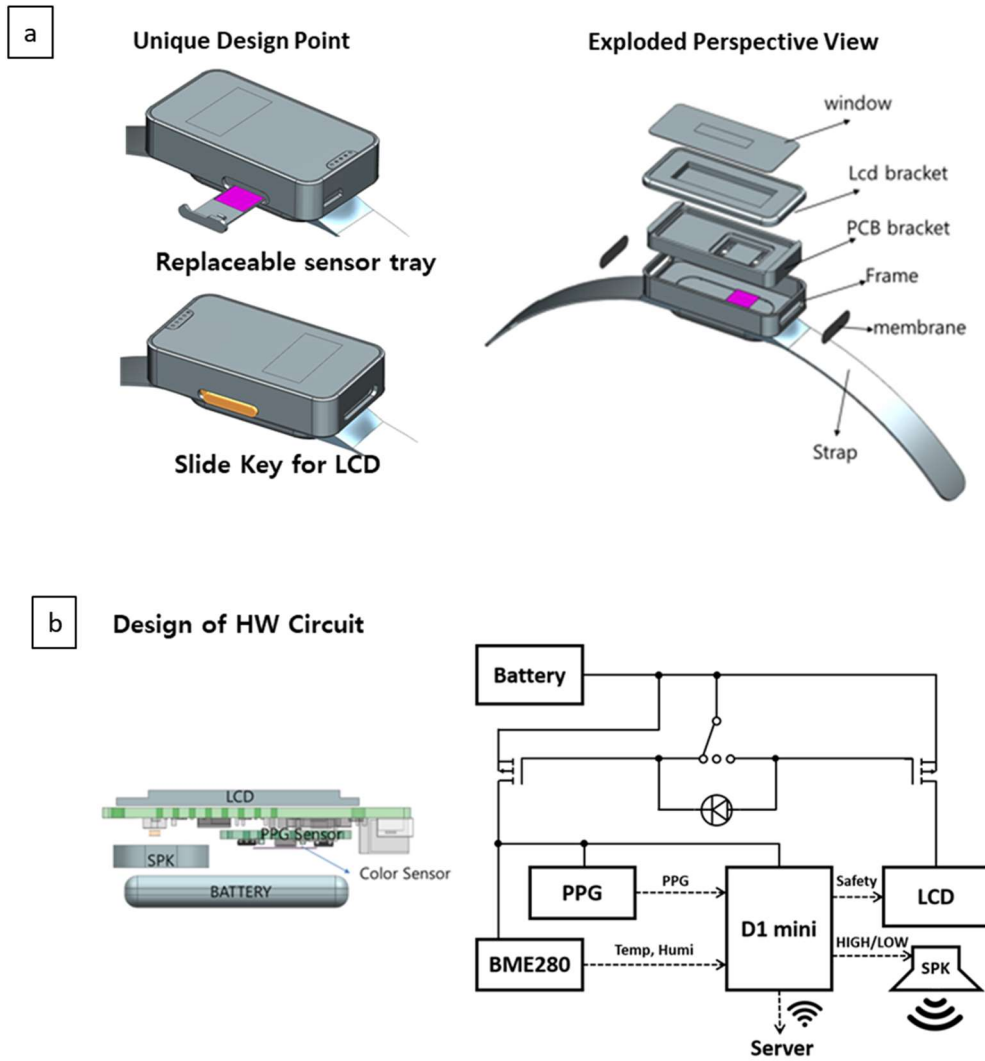
Figure 33. Design of wearable gas sensor (a) Unique design point using replaceable sensor tray and slide key for reducing power consumption, Exploded perspective view of designed watch type wearable gas sensor (b) Design of HW circuit and HW logic

	Display	Sensing Rate	SPK	LCD	WIFI	Power	Time
0 ~ 3PPM	Safe		OFF	OFF	OFF	1 mW ↓	72 H ↑
3 ~ 5 PPM	Warning	8 sec (initial 5 min)	ON	ON	ON	40 mW	4.5 H
5PPM ~	Danger		ON	ON	ON	41 mW	4 H

Table 6. Usage time of wearable gas sensor according to operating scenario

The design of the wearable gas sensor is as follows. The mechanical parts are divided into five sections. Figure 34a shows the teardown of a gas sensor fabricated in the form of a watch. The display window was implemented with an acrylic material coated with structural color. The LCD bracket and PCB bracket were manufactured using a 3D printer. The LCD, SPK, and switching PCB were assembled on the LCD bracket. The Arduino Mini, a humidity sensor (BME 280 for Arduino), and the PPG sensor (MAX 30102) were assembled on the PCB bracket. After the battery was assembled in the rear PC, it was attached to the rear metal. A separate rear metal and rear PC were used for WIFI communication. The next step was to combine the sub-assemblies, completing the watch production process. Figure 34b shows the gas-path design inside the wearable gas sensor. Owing to the nature of the wearable device, the internal design of the gas pipeline significantly affects the sensitivity of the wearable sensor, because the path through which gas passes is narrow. To extend the usage time, we improved the amount of gas flow by designing a gas path without thermal resistance. The LCD bracket was used to prevent harmful gas from penetrating the PCB, and it was designed to flow only between the battery and the gas sensor tray.

Figure 34. Teardown and Gas path design (a) Teardown of wearable gas sensor (b) Gas path design

An NO$_2$ gas test was conducted to validate the wearable gas sensor. The experiment was conducted using the manufactured experimental chamber, and the gas concentration was measured while controlling the NO$_2$ input using the MFC (Figure 35a). Gas was detected in the LCD ″on″ state by operating the slide key. Below 3 ppm, the message "SAFE" was displayed, and above 3 ppm, the message was changed to "WARNING" (Figure 35b).

Figure 36a shows the final operation diagram of the wearable gas sensor. The sensor transmitted data to and received data from the server using WIFI. Figure 36b shows the operation of the wearable gas sensor recorded by the server, which was confirmed using a smartphone application.
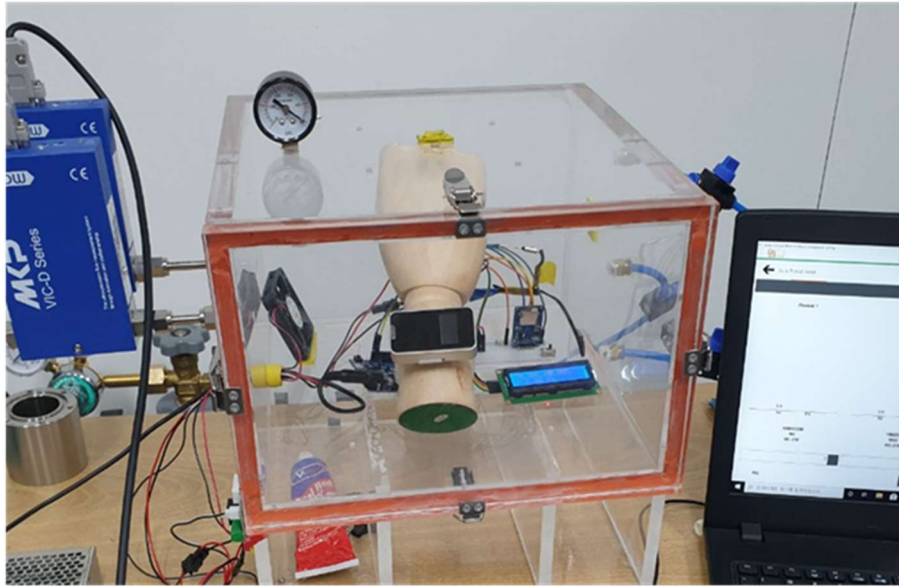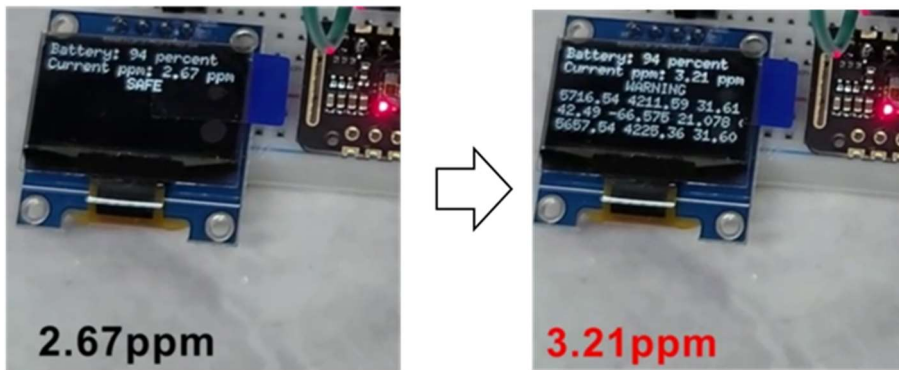
Figure 35. Experiment of wearable gas sensor (a) Gas experiment Setup (b) Gas path design
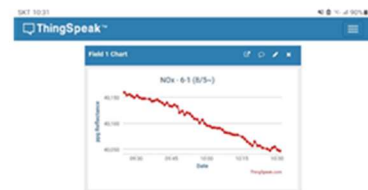
Figure 36. Wearable gas sensor scenario (a) Wearable Sensor algorithm (b) Communication with server using WIFI

Chapter 6. Conclusion

Recent advances in nano/microtechnology have led to active research on high-performance gas sensors. Advances in wearable gas sensors can lead to the application of gas sensors not only to protect workers from hazards but also to prevent accidents through continuous gas monitoring. In addition, they can protect humans from the long-term adverse effects of harmful gases and ensure safety in industrial environments.

In this study, we fabricated a colorimetric gas sensor with a simple FP-cavity structure. A new colorimetric NO_2 gas-sensing mechanism was developed, and simple e-beam evaporation with 90% yield was used for sensor fabrication. It was confirmed that the manufactured NO_2 gas sensor operates under the hazardous gas safety standards at room temperature. By combining this sensor with a low-power PPG sensor, the color change was converted into a quantified signal without expensive equipment or experts, and use of the PPG sensor allowed the detection of accumulated NO_2 gas at a level of 0.1 ppm.(Tables.7)

Using AI algorithms, we transformed the data into the real-time gas concentration, and gas sensing under 5 ppm with 95% reliability compared with commercial gas sensors was achieved (Figure 37). Additionally, a watch-type wearable gas sensor device was manufactured, and a real-time harmful-gas monitoring system can be developed through data communication. Finally, using the proposed device, a device capable of monitoring harmful gases without expensive equipment or expert help was demonstrated.
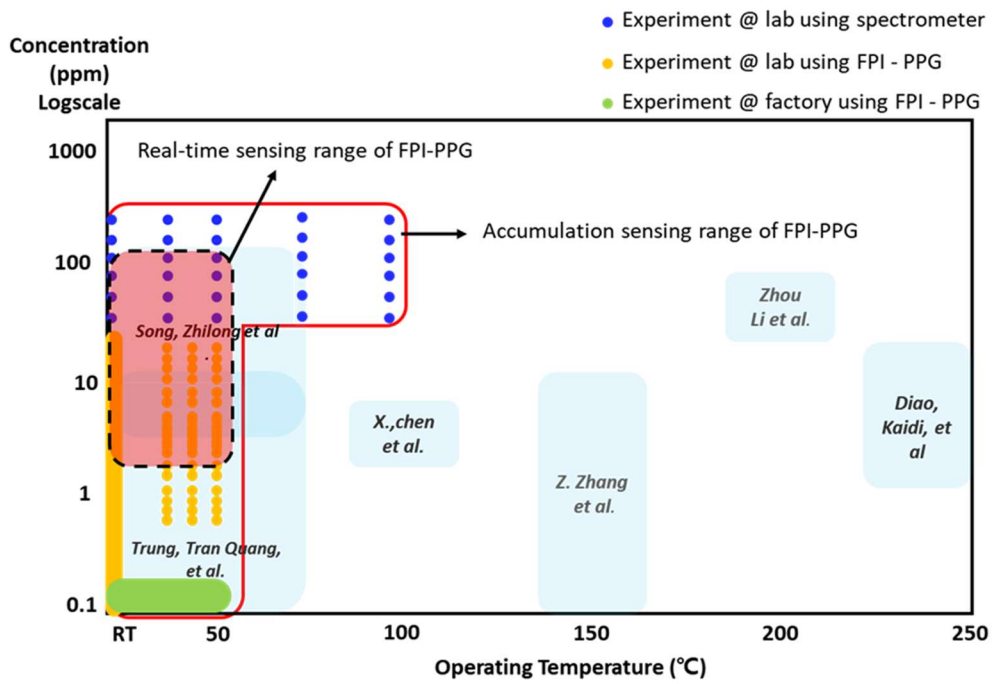
Figure 37. Sensing range of the combination of PPG sensor and NO_2 colorimetric gas sensor

Spec	Explanation	Sensor	Sensor Module
Resolution	Minimum detectable stimulus	-	0.1 ppm
Output format	-	Color	Reflectance
Fabrication Error	-	2.21 %	
Repeatability	**PPG (150 data of 6 conditions)**	**0.014%** **(2.79/20000)**	
Sensing Range	Accumulation (Hour)	-	0.1 ppm (Hour)
	Real-time (using AI)	-	5.0 ppm ~
Response time			8 sec (First : 320 sec)
Accuracy	Inaccuracy		1.34 ppm
Wearability	Room temp. (20 ~ 25 ℃)	OK	OK
	Low Power (Under 20 ~ 30mW)	0	Under 1 mW
	Small size	Under 200 nm	2 mm (PPG)

Tables 7 The specification of FPI−PPG NO_2 sensor

93

Bibliography

1.   Seo, Min-Ho, et al. "Chemo-Mechanically Operating Palladium-Polymer Nanograting Film for a Self-Powered H2 Gas Sensor." ACS nano 14.12 (2020): 16813-16822.

2.   Raghu, Appu Vengattoor, et al. "Wearable, flexible ethanol gas sensor based on TiO2 nanoparticles-grafted 2D-titanium carbide nanosheets." ACS Applied Nano Materials 2.3 (2019): 1152-1163.

3.   Ko, Kyung Yong, et al. "High-Performance Gas Sensor Using a Large-Area WS2 x Se2-2 x Alloy for Low-Power Operation Wearable Applications." ACS applied materials and interfaces 10.40 (2018): 34163-34171.

4.   Chang, Junyu, et al. "A Wearable Toxic Gas-Monitoring Device Based on Triboelectric Nanogenerator for Self-Powered Aniline Early Warning." Advanced Materials Technologies 5.5 (2020): 1901087.

5.   Tang, Yanting, et al. "Stretchable and wearable conductometric VOC sensors based on microstructured MXene/polyurethane core-sheath fibers." Sensors and Actuators B:

Chemical 346 (2021): 130500.

6.   Subbiah, Dinesh Kumar, et al. "Nanostructured ZnO on cotton fabrics–A novel flexible gas sensor and UV filter." Journal of Cleaner Production 194 (2018): 372−382.

7.   Zhu, Ling, and Wen Zeng. "Room−temperature gas sensing of ZnO−based gas sensor: A review." Sensors and Actuators A: Physical 267 (2017): 242−261.

8.   Bag, Atanu, and Nae-Eung Lee. "Recent Advancements in Development of Wearable Gas Sensors." Advanced Materials Technologies 6.3 (2021): 2000883.

9.   https://insideevs.com/

10.   https://news.naver.com/

11.   http://www.moel.go.kr/policy/policyinfo/workplace/list12.do

12.   Ho, Clifford K., and Robert C. Hughes. "In−situ chemiresistor sensor package for real−time detection of volatile organic compounds in soil and groundwater." Sensors 2.1 (2002): 23−34.

13.   www.figaro.co.jp

14.   Cho, Sung Hwan, et al. "Colorimetric sensors for toxic and hazardous gas detection: A review." Electronic Materials Letters (2020): 1−17.

15.   Kim, Young−Gyun, et al. "Lithography−free and Highly

Angle Sensitive Structural Coloration Using Fabry–Perot Resonance of Tin." International Journal of Precision Engineering and Manufacturing–Green Technology 8.3 (2021): 997−1006.

16.   Bariya, Mallika, Hnin Yin Yin Nyein, and Ali Javey. "Wearable sweat sensors." Nature Electronics 1.3 (2018): 160−171.

17.   Lee, Kyu-Tae, Sungyong Seo, and L. Jay Guo. "High-Color-Purity Subtractive Color Filters with a Wide Viewing Angle Based on Plasmonic Perfect Absorbers." Advanced Optical Materials 3.3 (2015): 347−352.

18.   Li, Zheng, and Kenneth S. Suslick. "Colorimetric sensor array for monitoring CO and ethylene." Analytical chemistry 91.1 (2018): 797−802.

19.   Kim, Young−Gyun, et al. "Nanoscale Ag/WO_3 Multilayered Fabry–Perot Cavities for Colorimetric NO_2 Sensing." ACS Applied Nano Materials (2021).

20.   Duan, Xiaoyang, Simon Kamin, and Na Liu. "Dynamic plasmonic colour display." Nature communications 8.1 (2017): 1−9.

21.   Sterl, Florian, et al. "Magnesium as novel material for active plasmonics in the visible wavelength range." Nano Letters 15.12 (2015): 7949−7955.

22.   Riaz, Farhan, et al. "Pervasive blood pressure monitoring

using Photoplethysmogram (PPG) sensor." Future Generation
Computer Systems 98 (2019): 120-130.

23.   Hong, John, et al. "Continuous color reflective displays using
interferometric absorption." Optica 2.7 (2015): 589-597.

24.   Wang, Hao, et al. "Full color generation using silver tandem
nanodisks." ACS nano 11.5 (2017): 4419-4427.

25.   Yang, Zhengmei, et al. "Reflective color filters and
monolithic color printing based on asymmetric Fabry-Perot cavities
using nickel as a broadband absorber." Advanced Optical Materials
4.8 (2016): 1196-1202.

26.   Kats, Mikhail A., et al. "Nanometre optical coatings based on
strong interference effects in highly absorbing media." Nature
materials 12.1 (2013): 20-24.

27.   Lee, Kyu-Tae, Sung Yong Han, and Hui Joon Park.
"Omnidirectional Flexible Transmissive Structural Colors with High-
Color-Purity and High-Efficiency Exploiting Multicavity
Resonances." Advanced Optical Materials 5.14 (2017): 1700284.

28.   Park, Sung-Ik, et al. "A review on fabrication processes for
electrochromic devices." International Journal of Precision
Engineering and Manufacturing-Green Technology 3.4 (2016):
397-421.

29.   https://support.lumerical.com/hc/en-us/articles/

30.   Pedrotti, Frank L., Leno M. Pedrotti, and Leno S. Pedrotti. Introduction to optics. Cambridge University Press, 2017.

31.   Kim, Young–Gyun, et al. "Lithography–free and Highly Angle Sensitive Structural Coloration Using Fabry–Perot Resonance of Tin." International Journal of Precision Engineering and Manufacturing–Green Technology 8.3 (2021): 997–1006.

32.   Kim, H. "Corrosion process of silver in environments containing 0.1 ppm H2S and 1.2 ppm NO₂." Materials and Corrosion 54.4 (2003): 243–250.

33.   Cho, Seong M., et al. "Design and fabrication of integrated fabry–perot type color reflector for reflective displays." Journal of Nanoscience and Nanotechnology 16.5 (2016): 5038–5043.

34.   Persad, Aaron H., and Charles A. Ward. "Expressions for the evaporation and condensation coefficients in the Hertz–Knudsen relation." Chemical reviews 116.14 (2016): 7727–7767.

35.   Pietilä, Julia, et al. "Evaluation of the accuracy and reliability for photoplethysmography based heart rate and beat–to–beat detection during daily activities." EMBEC and NBC 2017. Springer, Singapore, 2017. 145–148.

36.   Van Houdt, Greg, Carlos Mosquera, and Gonzalo Nápoles. "A review on the long short–term memory model." Artif. Intell. Rev. 53.8 (2020): 5929–5955.

37.   Baldi, Pierre, and Peter J. Sadowski. "Understanding dropout." Advances in neural information processing systems 26 (2013): 2814−2822.

요약 (국문초록)

페브리페로 구조 기반 웨어러블 컬러가스센서

김 영 균

서울대학교 기계항공공학부 기계전공 대학원

나노 마이크로 기술을 이용하여 고감도 가스 감지 물질이 개발되었으며, 이를 이용한 웨어러블 장치 형태의 가스 센서 개발은 유망한 연구 주제이다. 그러나 센서의 높은 전류 소비와 작동 온도를 극복하는 것은 많은 가스 감지 영역에서 여전히 과제로 남아 있다. 이를 개선하기 위해 센서 기술에 나노 패턴 구조의 구조적 착색을 이용한 컬러 가스 센서가 새로운 대안으로 떠오르고 있다. 그러나, 리소그래피 기반의 나노 패터닝 공정은 환경 친화적이지 않으며 이러한 접근 방식과 관련된 제한으로 인해 넓은 색상 영역을 제작하기가 어렵다. 또한 색 변화 측정, 데이터 정량화, 각도 의존성 등의 문제로 적용 확대에 어려움을 겪고 있으며, 컬러 센서에 대한 많은 연구에서 이 부분을 간과하고 있다.

본 연구에서는 나노 패터닝 공정이 필요하지 않은 Fabry-Perot 캐비티를 기반으로 상온에서 반응할 수 있는 컬러 가스 센서를 개발하였다.

FDTD를 이용하여 특정 파장에서 선형 변화 주기를 갖는 컬러 센서 소자를 설계하였다. 이러한 특성을 가진 컬러 센서와 간단한 측정 장치인 PPG 센서를 결합하여 저전력으로 신호를 정량화하는 메커니즘을 개발하였다.

센서 교체가 가능한 구조를 도입하여 다중 가스 감지 및 비가역 센서도 지속적으로 사용이 가능하게 하는 와치형 웨어러블 감지 장치를 제작하고, 그 결과 상온에서 NO_2 (0.1 ~ 500ppm)의 넓은 농도범위를 갖는 가스센서를 구현하였다. 최종적으로 상온에서 다층 컬러 필름을 이용하여 유해 가스를 감지하고, 저전력의 단색 LED를 이용하여 신호를 정량화하고 무선으로 통신할 수 있는 웨어러블 가스 센서의 가장 단순화된 설계를 제시하였다.

주요어 : 웨어러블 센서, 구조색, 페브리페롯, PPG센서, 박막필름, 컬러 가스 센서

학 번 : 2018-32205

101